Electronic Supplementary Information for

Molecular engineering nitrogen-rich helicene based organic semiconductors for stable perovskite solar cells

Yuefang Wei, Yaohang Cai, Lifei He, Yuyan Zhang, Yi Yuan,* Jing Zhang, and Peng Wang*

State Key Laboratory of Silicon and Advanced Semiconductor Materials, Department of Chemistry, Zhejiang University, Hangzhou 310030, China

E-mail: yyuan@zju.edu.cn; pw2015@zju.edu.cn

1. Experimental section

1.1. Materials

The following chemicals were obtained from commercial sources and utilized without additional purification: *N*-bromosuccinimide (NBS, 98% purity, Energy Chemical), sodium sulfite (97% purity, Energy Chemical), nitric acid (HNO$_3$, 65% purity, Sinopharm Chemical Reagent), sodium carbonate (Na$_2$CO$_3$, 98% purity, Energy Chemical), Pd/C (10 wt% on carbon, wetted with approximately 55% water, Energy Chemical), hydrazinium hydrate (85% purity, Sinopharm Chemical Reagent), tris(dibenzylideneacetone)dipalladium (Pd$_2$(dba)$_3$, 98% purity, Energy Chemical), tri-*tert*-butylphosphine tetrafluoroborate (P(*t*-Bu)$_3$·HBF$_4$, 98% purity, Energy Chemical), sodium *tert*-butoxide (NaO(*t*-Bu), 98% purity, Energy Chemical), 2,3-dichloro-5,6-dicyano-1,4-benzoquinone (DDQ, 98% purity, Energy Chemical), iodomethane (99.5% purity, Energy Chemical), sodium hydride (NaH, 60% purity, Energy Chemical), bis(4-methoxyphenyl)amine (98% purity, Energy Chemical), palladium(II) diacetate (Pd(OAc)$_2$, 99% purity, Energy Chemical), tri(*o*-tolyl)phosphine (P(*o*-tolyl)$_3$, 98% purity, Energy Chemical), pivalic acid (99% purity, Energy Chemical), potassium carbonate (K$_2$CO$_3$, 98% purity, Energy Chemical), 1-ethyl-3-methylimidazolium bis(trifluoromethanesulfonyl)imide (EMITFSI, 98% purity, Energy Chemical), bis(pentamethylcyclopentadienyl)iron (DMFc, 98% purity, ACROS), benzocyclobutene (BCB, 98% purity, Energy Chemical), tetrahydrofuran (THF, extra dry, 99.9% purity, Energy Chemical), trichloromethane (99% purity, Sinopharm Chemical Reagent), toluene (99% purity, Sinopharm Chemical Reagent), *N,N*-dimethylformamide (DMF, extra dry, 99.8% purity, Energy Chemical), deuterated chloroform (CDCl$_3$, 99.8% purity, Energy Chemical), deuterated tetrahydrofuran (THF-*d$_8$*, 99.8% purity, Energy Chemical), isopropanol (IPA, ≥ 99.9% purity, Energy Chemical), chlorobenzene (CB, 99.8% purity, Acros Organics), 4-*tert*-butylpyridine (TBP, 96% purity, Aldrich), acetone (≥ 99.5% purity, Energy Chemical), ethanol (99.7% purity, Aladdin), zinc iodide (ZnI$_2$, 99.995% purity, Alfa Aesar), hexakis(methoxymethyl)melamine (≥ 98% purity, Macklin), titanium diisopropoxide bis(acetylacetonate) (TIACA, 75% in isopropanol, Aldrich), acetylacetone (ACAC, > 99.0% purity, TCI), TiO$_2$ paste (30NR-D, Greatcell Solar), PbI$_2$ (99.99% purity, TCI), PbBr$_2$ (99.99% purity, TCI), formamidinium iodide (FAI, 99.0% purity, Greatcell Solar), methylammonium bromide (MABr, 99.0% purity, Greatcell Solar), CsI (99.0% purity, TCI), dimethyl sulfoxide (DMSO, 99.9% purity, Aldrich), and spiro-OMeTAD (99.8% purity, Xi'an Polymer Light Technology Corp.). The compounds 7-methyl-7*H*-dibenzo[*c*,*g*]carbazole (**1**),[1] 4-(2,3-dihydrothieno[3,4-*b*][1,4]dioxin-5-yl)-*N*,*N*-bis(4-methoxyphenyl)aniline,[2] and 4-*tert*-butylpyridinium bis(trifluoromethanesulfonyl)imide (TBPHTFSI)[3] were synthesized using the procedures outlined in the literatures.

1.2. General characterization

Melting points were determined using a WRS-1B automatic digital melting point apparatus (Shanghai INESA Physico-

Optical Instrument). ^{1}H NMR and ^{13}C NMR spectra were acquired on an AVANCE III 400 NMR spectrometer (Bruker). High-resolution mass spectra (HR-MS) were obtained using a MALDI-TOF spectrometer (Bruker) or a 6545 LC/Q-TOF system (Agilent). Attenuated total reflection-Fourier transform infrared (ATR-FTIR) spectra were recorded using a Vector 22 FTIR spectrometer (Bruker). Cyclic voltammetry (CV) measurements were conducted on a CHI660C electrochemical workstation (CH Instruments) with a three-electrode electrolytic cell, comprising a glassy carbon working electrode, a platinum foil counter electrode, and an Ag/AgCl (sat. KCl) reference electrode. The supporting electrolyte consisted of a 0.1 M solution of EMITFSI in THF. Ultraviolet-visible (UV-Vis) absorption spectra were collected using a Cary 8454 spectrophotometer (Agilent Technologies). Time-resolved photoluminescence (TRPL) decays were acquired using a Life-Spec-II fluorescence spectrometer (Edinburgh Instruments Ltd). Differential scanning calorimetry (DSC) measurements were performed using a DSC Q100 V9.7 Build 291 instrument (TA) under a flowing nitrogen atmosphere with a heating rate of 10 $^\circ$C min^{-1}. Contact angles of water droplets on thin films were measured using a Dropmeter 100P contact angle meter (Maist Co. Ltd.). Polarization optical microscope (POM) images were captured using an SDPTOP CX40P system (Sunny Optical Technology). X-ray diffraction (XRD) patterns of thin film were measured with a SmartLab diffractometer (Rigaku), using Cu Kα radiation (λ = 0.15418 nm) operated at 7200 W power (40 kV, 180 mA). Fluorescence optical microscope (FOM) images were recorded with an ECLIPSE Ti-U system (Nikon). Scanning electron microscope (SEM) images were obtained using a SU-70 field emission scanning electron microscope (Hitachi).

1.3. Synthesis

1.3.1. 5-Bromo-7-methyl-7*H*-dibenzo[*c,g*]carbazole (2)

A solution of 7-methyl-7*H*-dibenzo[*c,g*]carbazole (**1**) (2.81 g, 10.00 mmol) in 20 mL of THF was subjected to dropwise addition of a solution of NBS (2.37 g, 13.33 mmol) in 15 mL of THF at a temperature of −20 $^\circ$C. Following stirring at this temperature for 30 min, the reaction was quenched using a 0.1 M aqueous solution of sodium sulfite (30 mL). Subsequently, the resulting mixture was subjected to extraction with three portions of dichloromethane (50 mL each). The organic layers were combined, and the solvent was removed under reduced pressure. The crude product was further purified by column chromatography on silica gel using a mixture of THF and petroleum ether (60−90 $^\circ$C, *v/v*, 1/20) as the eluent. This process afforded a white solid as the desired product **2** (2.34 g, 65% yield). Melting point: 141−142 °C. ^{1}H NMR (400 MHz, CDCl$_3$) δ: 9.04 (d, *J* = 8.5 Hz, 1H), 8.97 (d, *J* = 8.5 Hz, 1H), 8.32 (d, *J* = 8.4 Hz, 1H), 7.89 (d, *J* = 8.1 Hz, 1H), 7.84 (s, 1H), 7.75 (d, *J* = 8.9 Hz, 1H), 7.57 – 7.43 (m, 4H), 7.37 (t, *J* = 7.5 Hz, 1H), and 3.79 (s, 3H) ppm. ^{13}C NMR (100 MHz, CDCl$_3$) δ: 137.69, 137.04, 129.74, 129.65, 129.17, 128.87, 128.21, 127.32, 127.06, 125.98, 125.55, 125.22, 124.81, 124.25, 123.38, 120.11, 117.11, 116.71, 114.96, 110.48, and 29.46 ppm. HR-MS (ESI) *m/z* calculated for [M]$^+$: 359.0310. Found: 359.0304. ATR-FTIR (film) v_{max}: 3041, 2925, 1603, 1573, 1525, 1466, 1375, 1323, 1196, 1154, 1007, 937, 855, 798, and 742 cm^{-1}.

1.3.2. 7-Methyl-5-nitro-7*H*-dibenzo[*c,g*]carbazole (3)

A trichloromethane solution (30 mL) containing compound **1** (2.81 g, 10.00 mmol) underwent dropwise addition of HNO_3 (0.69 mL, 10.50 mmol). The resulting mixture was stirred at room temperature for 2 h, followed by neutralization with a 0.1 M aqueous solution of sodium carbonate (10 mL). Subsequently, the mixture was transferred to 50 mL of deionized water and subjected to extraction with three portions of dichloromethane (50 mL each). The organic layers were combined and washed with 100 mL of deionized water. Evaporation of the solvent under reduced pressure yielded an orange solid as the desired product **3** (3.20 g, 98% yield). Melting point: 205–206 °C. ^{1}H NMR (400 MHz, CDCl$_3$) δ: 9.18 – 9.11 (m, 1H), 9.00 (d, J = 8.4 Hz, 1H), 8.82 – 8.72 (m, 1H), 8.52 (s, 1H), 8.03 (d, J = 8.0 Hz, 1H), 7.97 (d, J = 8.9 Hz, 1H), 7.76 – 7.59 (m, 4H), 7.58 – 7.52 (m, 1H), and 4.05 (s, 3H) ppm. ^{13}C NMR (100 MHz, CDCl$_3$) δ: 143.62, 140.66, 133.99, 129.88, 129.53, 129.42, 128.95, 128.93, 126.36, 126.20, 126.05, 125.24, 124.69, 124.24, 124.16, 121.97, 121.43, 116.37, 110.49, 110.12, and 29.77 ppm. HR-MS (ESI) *m/z* calculated for [M+Na]$^+$: 349.0947. Found: 349.0949. ATR-FTIR (film) v_{max}: 2926, 1609, 1532, 1504, 1467, 1441, 1386, 1316, 1254, 1202, 1159, 1124, 1066, 1014, 830, 800, and 767 cm^{-1}.

1.3.3. 7-Methyl-7*H*-dibenzo[*c,g*]carbazol-5-amine (4)

A solution of compound **3** (1.63 g, 5.00 mmol) in THF was vigorously stirred, followed by the addition of Pd/C (10 wt%, 163 mg). Subsequently, hydrazinium hydrate (0.71 mL, 12.50 mmol) was carefully added dropwise. The resulting mixture was stirred at room temperature for 30 min, after which Pd/C was filtered out and the solvent was evaporated under vacuum. Purification of the crude product involved column chromatography (THF/petroleum ether 60–90 °C, *v/v*, 2/1) on neutral aluminum oxide. This process yielded a light yellow solid as the desired product **4** (1.36 g, 92% yield). Melting point: 165–166 °C. ^{1}H NMR (400 MHz, THF-d_8) δ: 9.04 (t, J = 7.4 Hz, 2H), 8.03 (d, J = 8.4 Hz, 1H), 7.86 (d, J = 8.1 Hz, 1H), 7.73 – 7.56 (m, 2H), 7.53 – 7.38 (m, 2H), 7.37 – 7.09 (m, 2H), 6.85 (s, 1H), 5.13 (s, 2H), and 3.96 (s, 3H) ppm. ^{13}C NMR (100 MHz, THF-d_8) δ: 144.87, 141.08, 137.84, 131.18, 131.07, 129.92, 129.65, 126.11, 125.93, 125.86, 125.18, 124.69, 123.75, 123.24, 122.56, 118.88, 111.33, 110.75, 93.15, and 29.49 ppm. HR-MS (ESI) *m/z* calculated for [M]$^+$: 296.1313. Found: 296.1308. ATR-FTIR (film) v_{max}: 3361, 3233, 3039, 2925, 2865, 1616, 1528, 1466, 1435, 1399, 1376, 1326, 1257, 1208, 1061, 1008, 900, 800, and 748 cm^{-1}.

1.3.4. Bis(7-methyl-7*H*-dibenzo[*c,g*]carbazol-5-yl)amine (5)

Compound **2** (1.80 g, 5.00 mmol), compound **4** (1.48 g, 5.00 mmol), Pd$_2$(dba)$_3$ (137 mg, 0.15 mmol), P(t-Bu)$_3$·HBF$_4$ (87 mg, 0.30 mmol), NaO(*t*-Bu) (721 mg, 7.50 mmol), and toluene (50 mL) were added to a dried Schlenk tube. The tube was subsequently evacuated and purged with argon three times. The reaction mixture was refluxed under argon for 12 h. After cooling, the mixture was filtered through a Kieselguhr pad. The filtrate was then concentrated under vacuum and subjected to purification by column chromatography (THF/petroleum ether 60 – 90 °C, *v/v*, 1/2) using neutral aluminum oxide. This

process yielded a light yellow solid as the desired product **5** (2.50 g, 87% yield). Melting point: 266–267 °C. ^{1}H NMR (400 MHz, THF-d_8) δ: 9.28 (d, J = 8.6 Hz, 2H), 9.23 (d, J = 8.5 Hz, 2H), 8.52 (d, J = 8.4 Hz, 2H), 8.08 – 7.93 (m, 3H), 7.83 (d, J = 8.9 Hz, 2H), 7.76 (d, J = 8.9 Hz, 2H), 7.68 (t, J = 7.7 Hz, 2H), 7.61 (t, J = 7.6 Hz, 2H), 7.50 – 7.34 (m, 6H), and 3.85 (s, 6H) ppm. ^{13}C NMR (100 MHz, THF-d_8) δ: 141.83, 139.89, 138.67, 131.33, 131.15, 130.10, 129.92, 126.36, 126.30, 126.13, 125.84, 125.71, 125.51, 125.00, 123.66, 123.58, 118.40, 113.99, 111.59, 101.83, and 29.56 ppm. HR-MS (MALDI-TOF) m/z calculated for [M]$^+$: 575.2362. Found: 575.2362. ATR-FTIR (film) ν_{max}: 3393, 2924, 2856, 1722, 1586, 1528, 1464, 1399, 1366, 1324, 1278, 1249, 1153, 1064, 1008, 905, 798, and 748 cm^{-1}.

1.3.5.   20,21-Dimethyl-20,21-dihydro-9*H*-dibenzo[*a,i*]benzo[4,5]indolo[3,2-*c*]benzo[4,5]indolo[2,3-*g*]carbazole (DMDAP)

A solution of compound **5** (2.30 g, 4.00 mmol) in toluene (50 mL) was prepared, to which DDQ (908 mg, 4.00 mmol) was added. After stirring at room temperature for 30 min, the mixture was filtered through a silica gel pad. Subsequently, the solvent was evaporated under vacuum to obtain the crude product. Purification of the crude product involved column chromatography (THF/petroleum ether 60 – 90 °C, *v/v*, 1/1) using silica gel as the stationary phase. This process yielded a white solid as the desired product DMDAP (1.83 g, 80% yield). Melting point: > 300 °C. ^{1}H NMR (400 MHz, THF-d_8) δ: 12.25 (s, 1H), 9.37 – 9.33 (m, 2H), 9.13 (d, J = 8.4 Hz, 2H), 8.84 – 8.76 (m, 2H), 8.06 (d, J = 7.6 Hz, 2H), 7.95 – 7.88 (m, 4H), 7.68 – 7.58 (m, 6H), 7.49 (t, J = 7.2 Hz, 2H), and 4.24 (s, 6H) ppm. ^{13}C NMR (100 MHz, THF-d_8) δ: 140.36, 137.78, 136.14, 131.82, 129.99, 129.83, 129.57, 126.69, 125.95, 125.85, 125.71, 125.51, 124.18, 124.05, 123.08, 120.59, 120.22, 115.20, 112.70, 107.32, and 34.34 ppm. HR-MS (ESI) m/z calculated for [M]$^+$: 573.2205. Found: 573.2199. ATR-FTIR (film) ν_{max}: 3312, 2969, 2858, 1611, 1522, 1461, 1381, 1327, 1260, 1064, 901, 801, and 745 cm^{-1}.

1.3.6.   9,20,21-Trimethyl-20,21-dihydro-9*H*-dibenzo[*a,i*]benzo[4,5]indolo[3,2-*c*]benzo[4,5]indolo[2,3-*g*]carbazole (TMDAP)

A solution of DMDAP (1.72 g, 3.00 mmol) in dry DMF (50 mL) was prepared, followed by the addition of NaH (132 mg, 3.30 mmol) and iodomethane (0.13 mL, 3.15 mmol). The mixture was stirred at room temperature for 3 h. To quench the reaction, 5 mL of methanol was slowly added. The resulting mixture was then transferred to deionized water (50 mL) and subjected to extraction with three portions of dichloromethane (50 mL each). The organic layers were combined, and the solvent was subsequently evaporated under vacuum. Purification of the crude product was carried out by column chromatography (THF/petroleum ether 60 – 90 °C, *v/v*, 1/2) using silica gel as the stationary phase. This process yielded a white solid as the desired product TMDAP (1.73 g, 98% yield). Melting point: > 300 °C. ^{1}H NMR (400 MHz, THF-d_8) δ: 9.24 – 9.16 (m, 2H), 8.98 (d, J = 6.9 Hz, 2H), 8.69 – 8.60 (m, 2H), 7.85 (d, J = 6.4 Hz, 2H), 7.70 (d, J = 7.2 Hz, 2H), 7.66 (d, J = 7.1 Hz, 2H), 7.47 – 7.37 (m, 6H), 7.30 – 7.23 (m, 2H), 4.76 (s, 3H), and 4.07 (s, 6H) ppm. ^{13}C NMR (100 MHz, THF-

d_8) δ: 140.59, 137.20, 131.83, 130.44, 130.07, 129.84, 129.82, 129.07, 126.57, 126.47, 126.13, 125.63, 125.38, 124.96, 124.10, 121.44, 120.08, 115.89, 112.71, 108.25, 42.93, and 34.34 ppm. HR-MS (MALDI-TOF) m/z calculated for $[M]^+$: 587.23615. Found: 587.23458. ATR-FTIR (film) ν_{max}: 2957, 2922, 2852, 1740, 1653, 1540, 1522, 1459, 1378, and 1076 cm^{-1}.

1.3.7. 18,23-Dibromo-9,20,21-trimethyl-20,21-dihydro-9*H*-dibenzo[*a,i*]benzo[4,5]indolo[3,2-*c*]benzo[4,5]indolo[2,3-*g*]carbazole (TMDAPBr$_2$)

A solution of compound TMDAP (1.47 g, 2.50 mmol) in THF (50 mL) was prepared, and NBS (979 mg, 5.50 mmol) was added at 0 °C. After stirring at 0 °C for 1 h, the mixture was quenched with a sodium sulfite aqueous solution (0.1 M, 30 mL). The resulting mixture was transferred to deionized water (50 mL) and subjected to extraction with three portions of dichloromethane (50 mL each). The organic layers were combined, and the solvent was subsequently evaporated under vacuum. Purification of the crude product was achieved by column chromatography (THF/petroleum ether 60 – 90 °C, *v/v*, 1/3) using silica gel as the stationary phase. This process yielded a yellow solid as the desired product TMDAPBr$_2$ (1.79 g, 96% yield). Melting point: > 300 °C. ^{1}H NMR (400 MHz, THF-d_8) δ: 9.32 – 9.28 (m, 2H), 9.19 (d, J = 8.3 Hz, 2H), 8.87 – 8.78 (m, 2H), 8.47 (d, J = 8.3 Hz, 2H), 8.28 (s, 2H), 7.77 – 7.67 (m, 2H), 7.66 – 7.54 (m, 6H), 4.82 (s, 3H), and 4.09 (s, 6H) ppm. ^{13}C NMR (100 MHz, THF-d_8) δ: 140.78, 140.23, 137.48, 130.38, 130.18, 129.20, 129.01, 126.85, 126.48, 126.38, 125.70, 125.50, 125.07, 124.48, 121.54, 120.21, 119.25, 117.42, 115.54, 107.94, 42.88, and 34.41 ppm. HR-MS (MALDI-TOF) m/z calculated for $[M]^+$: 745.05513. Found: 745.05504. ATR-FTIR (film) ν_{max}: 2955, 2923, 2853, 1462, 1371, 1330, 1258, and 751 cm^{-1}.

1.3.8. $N^{18},N^{18},N^{23},N^{23}$-Tetrakis(4-methoxyphenyl)-9,20,21-trimethyl-20,21-dihydro-9*H*-dibenzo[*a,i*]benzo[4,5]indolo[3,2-*c*]benzo[4,5]indolo[2,3-*g*]carbazole-18,23-diamine (TMDAP-OMeDPA)

Compound TMDAPBr$_2$ (746 mg, 1.00 mmol), bis(4-methoxyphenyl)amine (573 mg, 2.50 mmol), Pd$_2$(dba)$_3$ (46 mg, 0.05 mmol), P(*t*-Bu)$_3$·HBF$_4$ (29 mg, 0.10 mmol), NaO(*t*-Bu) (288 mg, 3.00 mmol), and toluene (30 mL) were introduced into a dried Schlenk tube. The tube was subsequently evacuated and purged with argon three times. The reaction mixture was then refluxed under argon for 12 h. After cooling, the mixture was filtered through a Kieselguhr pad. The resulting filtrate was concentrated under vacuum and subjected to purification by column chromatography (THF/petroleum ether 60 – 90 °C, *v/v*, 1/1) using silica gel as the stationary phase. This process yielded a yellow solid as the desired product TMDAP-OMeDPA (886 mg, 85% yield). Melting point: > 300 °C. ^{1}H NMR (400 MHz, THF-d_8) δ: 9.33 – 9.23 (m, 2H), 9.07 (d, J = 8.4 Hz, 2H), 8.79 – 8.71 (m, 2H), 8.12 (d, J = 8.1 Hz, 2H), 7.58 (s, 2H), 7.54 – 7.42 (m, 6H), 7.23 (t, J = 7.4 Hz, 2H), 7.00 (d, J = 9.0 Hz, 8H), 6.77 (d, J = 9.0 Hz, 8H), 4.91 (s, 3H), 4.07 (s, 6H), and 3.69 (s, 12H) ppm. ^{13}C NMR (100 MHz, THF-d_8) δ: 155.79, 143.94, 142.58, 140.83, 140.64, 137.69, 131.07, 130.20, 129.41, 126.93, 126.66, 126.46, 125.75,

125.40, 125.03, 124.48, 124.19, 123.73, 121.43, 118.76, 115.93, 115.31, 113.83, 108.26, 55.68, 43.10, and 34.40 ppm. HR-MS (MALDI-TOF) *m/z* calculated for [M]$^+$: 1041.4254. Found: 1041.4249. ATR-FTIR (film) v_{max}: 2956, 2922, 2852, 1503, 1459, 1365, 1238, 1177, 979, 825, and 755 cm^{-1}.

1.3.9. **4,4'-((9,20,21-Trimethyl-20,21-dihydro-9*H*-dibenzo[*a,i*]benzo[4,5]indolo[3,2-*c*]benzo[4,5]indolo[2,3-*g*]carbazole-18,23-diyl)bis(2,3-dihydrothieno[3,4-*b*][1,4]dioxine-7,5-diyl))bis(*N,N*-bis(4-methoxyphenyl)aniline) (TMDAP-EP-OMeDPA)**

A dried Schlenk tube was charged with compound TMDAPBr$_2$ (746 mg, 1.00 mmol), 4-(2,3-dihydrothieno[3,4-*b*][1,4]dioxin-5-yl)-*N,N*-bis(4-methoxyphenyl)aniline (1.11 g, 2.50 mmol), Pd(OAc)$_2$ (11 mg, 0.05 mmol), P(*o*-tolyl)$_3$ (30 mg, 0.10 mmol), pivalic acid (20 mg, 0.20 mmol), K$_2$CO$_3$ (415 mg, 3.00 mmol), and DMF (50 mL). The tube was then evacuated and purged with argon three times. The reaction mixture was stirred at 130 ºC under argon for 24 h. After cooling, the mixture was filtered through a Kieselguhr pad. The filtrate was concentrated under vacuum and subjected to purification by column chromatography (THF/petroleum ether 60 – 90 ºC, *v/v*, 1/1) using silica gel as the stationary phase. This process yielded a yellow solid as the desired product TMDAP-EP-OMeDPA (1.27 g, 86% yield). Melting point: > 300 °C. ^{1}H NMR (400 MHz, THF-*d$_8$*) δ: 9.53 – 9.44 (m, 2H), 9.28 (d, *J* = 6.8 Hz, 2H), 9.02 – 8.91 (m, 2H), 8.36 (d, *J* = 6.8 Hz, 2H), 8.05 (s, 2H), 7.78 – 7.62 (m, 10H), 7.55 (t, *J* = 6.1 Hz, 2H), 7.10 (d, *J* = 7.2 Hz, 8H), 6.96 (d, *J* = 7.1 Hz, 4H), 6.90 (d, *J* = 7.2 Hz, 8H), 4.93 (s, 3H), 4.39 – 4.33 (m, 4H), 4.29 – 4.26 (m, 4H), 4.19 (s, 6H), and 3.75 (s, 12H) ppm. ^{13}C NMR (100 MHz, THF-*d$_8$*) δ: 157.96, 157.35, 149.72, 148.40, 141.92, 140.74, 140.19, 139.90, 138.45, 137.69, 130.37, 130.00, 128.93, 128.04, 127.54, 127.42, 126.84, 126.64, 126.47, 125.59, 125.04, 124.27, 121.54, 121.44, 120.28, 117.72, 115.83, 115.60, 115.51, 113.41, 108.26, 65.89, 65.58, 65.56, 55.76, and 34.41 ppm. HR-MS (MALDI-TOF) *m/z* calculated for [M]$^+$: 1474.4778. Found: 1474.4771. ATR-FTIR (film) v_{max}: 2957, 2923, 2853, 1741, 1652, 1540, 1513, 1458, 1421, 1370, and 1087 cm^{-1}.

1.4. Conductivity

A hole transport layer was deposited onto interdigital gold electrodes by spin-coating a chlorobenzene solution at 1000 rpm. The solution consisted of 35 mg mL^{-1} of organic semiconductor and TBPHTFSI at concentrations of 0, 1.8, 3.9, and 6.2 mg mL^{-1}. The interdigital gold electrode consisted of 119 channels, each with a length (*L*) of 1.5 mm, a width (*W*) of 10 μm, and a thickness (*t*) of 110 nm. Prior to measuring the current–voltage (*I–V*) curve using a Keithley 2400 source meter, the sample was stored in dry air (< 5% RH) for seven days. The *I–V* curve was measured in the voltage range from −1.0 V to 1.0 V. The direct-current conductivity (σ) was calculated using the equation $\sigma = s\dfrac{W}{nLt}$, where s represents the slope derived from the linear fitting of the *I–V* curve and n is the channel number. It is noteworthy that the hole transport

layer's conductivity (σ) reached a steady state after being stored in dry air for approximately five days and remained constant thereafter, suggesting that air doping had reached equilibrium.

1.5. Hole density

We employed a metal-insulator-semiconductor (MIS) device to quantify the hole density within the hole transport layer (HTL), exclusively composed of organic semiconductor molecules. The MIS device architecture used in this study consisted of n^{++}-Si/SiO$_2$/p-BCB/HTL/Au, with p-BCB representing polybenzocyclobutene. To prepare the p-BCB layer, a 1 mg mL^{-1} solution of BCB in CB was spin-coated onto heavily n-type doped Si with a 300 nm SiO$_2$ coating. The BCB layer was then annealed at 250 $^{\circ}$C for 30 min, resulting in the growth of the p-BCB layer. Subsequently, the HTL was spin-coated onto the p-BCB layer, followed by the deposition of a gold layer using vacuum deposition techniques.

Impedance spectra of the MIS device were measured at various bias potentials (V) using an AutolabPGSTAT302N electrochemical workstation. The capacitance (C) was computed using the equation $C = -\dfrac{1}{\omega}[\dfrac{Z''-\omega L_{\mathrm{i}}}{(Z'-R_{\mathrm{s}})^2+(Z''-\omega L_{\mathrm{i}})^2}]$, where Z' and Z'' represent the real and imaginary parts of the impedance spectra, respectively. R_{s} represents the series resistance, L_{i} denotes the parasitic inductance, and ω is the angular frequency. The C–V feature clearly exhibited the accumulation and depletion regimes of the organic semiconductor layer. Subsequently, the hole density (p) was calculated as $p = \dfrac{2}{q\varepsilon_{\mathrm{r}}\varepsilon_0 \dfrac{d(A/C)^2}{dV}}$, where q represents the elementary charge, ε_{r} refers to the relative permittivity, ε_0 denotes the vacuum permittivity, and A represents the area of the MIS device.

In subsequent experiments, determining the hole density of a hole transport layer containing TBPHTFSI using the MIS device proved to be challenging. To overcome this obstacle, we employed a comparison approach by analyzing the quadratic integral intensity of the electron paramagnetic resonance (EPR) signal from the hole transport layer with or without TBPHTFSI. By utilizing the known density of the layer without TBPHTFSI as a reference, we estimated the hole density. For this purpose, a HTL was spin-coated onto a 2 cm × 2 cm microslide and stored in dry air for seven days. The resulting sample was then crushed and loaded into a borosilicate glass tube for EPR measurement using an A300-10/12 spectrometer (Bruker).

1.6. Fabrication of solar cells

A pre-cleaned fluorine-doped tin oxide (FTO) glass substrate was employed for depositing a compact TiO$_2$ (c-TiO$_2$) layer through spray pyrolysis, utilizing an ethanolic solution of TIACA and ACAC. Subsequently, a spin-coating technique was utilized to apply a mesoporous TiO$_2$ (m-TiO$_2$) layer, approximately 200 nm thick, onto the c-TiO$_2$ layer using an ethanolic solution of TiO$_2$ colloid formulated with commercial 30NR-D TiO$_2$ paste. The resulting film was sintered at 450 $^{\circ}$C, yielding the TiO$_2$-coated FTO electrode.

To prepare the CsMAFA perovskite precursor solution, a mixture of DMSO and DMF (v/v, 1/4) was combined with 1.30 M of PbI_2, 0.14 M of $PbBr_2$, 1.19 M of FAI, 0.14 M of MABr, and 0.07 M of CsI. Subsequently, the precursor solution was deposited onto the c-TiO_2/m-TiO_2 substrate through a two-step spin-coating process: 1000 rpm for 10 s (ramp rate 200 rpm s^{-1}) and 6000 rpm for 30 s (ramp rate 2000 rpm s^{-1}). At 15 s before the completion of the program, 150 μL of chlorobenzene was introduced onto the spinning substrate. The film was then annealed at 120 °C for 30 min, resulting in the formation of the CsMAFA perovskite film.

Next, 50 μL of an IPA solution of ZnI_2 (4 mg mL^{-1}) was deposited onto the perovskite film and spin-coated at 3000 rpm for 30 s. The film was subsequently annealed at 80 °C. Following this, 50 μL of an IPA solution of HMMM (2 mg mL^{-1}) was spin-coated onto the perovskite layer at 3000 rpm for 30 s, followed by annealing at 80 °C for 30 min.

The hole transport layer (HTL) solution, approximately 60 nm thick, was then spin-coated at 5000 rpm for 30 s with a ramp rate of 2000 rpm s^{-1}. The chlorobenzene solution comprised 35 mg mL^{-1} of an organic semiconductor, along with 6.18 mg mL^{-1} of TBPHTFSI and 132 mM TBP.

Finally, an 80 nm-thick gold layer was thermally evaporated under a vacuum of $\leq 1 \times 10^{-4}$ Pa. The samples were cautiously covered with waterproof adhesive tape and further sealed with a 3M epoxy adhesive.

1.7. Photocurrent−voltage and external quantum efficiency measurements

We characterized perovskite solar cells using an LS1000-4S-AM solar simulator (Solar Light Company) to deliver AM1.5G sunlight at an irradiation level of 100 mW cm^{-2}. The photocurrent density-voltage ($J–V$) curves were measured with a Keithley 2400 source meter controlled by a custom Labview 14.0 program. The photoactive area of the perovskite solar cells was defined by a precisely measured aperture area of 0.16 cm^2 using a black metal mask calibrated at the National Institute of Metrology. To evaluate the external quantum efficiency (EQE) spectra, photocurrent measurements were performed under short circuit conditions using a computer-controlled Keithley 2400 source meter and an Omni-λ300 monochromator (Zolix). The intensity of monochromatic light was determined by a Hamamatsu S1337-1010BQ silicon diode calibrated at the National Institute of Metrology, China.

1.8. Operational stability and thermostability

To perform maximum power point (MPP) tracking of perovskite solar cells, a 16-channel photovoltaic tracking system (YH Electronic Equipment Business) was utilized in combination with an SLS-LED-80A solar simulator (Qingdao Solar Scientific Instrument High-tech Co., LTD). This experiment was conducted within a nitrogen-filled glovebox to maintain controlled conditions. The MPP data were collected at 30 min intervals using the perturb and observe method, ensuring precise tracking of the performance parameters at MPP.

To assess the thermostability of the perovskite solar cells, they were subjected to an FD56 oven (Binder) set at 85 °C. The atmospheric humidity outside the oven varied between 40% and 90%. Periodic *J–V* measurements were performed under AM1.5G conditions to continuously monitor the performance parameters.

2. Theoretical modelling

2.1. Frontier molecular orbital

We optimized the molecular geometry by the density functional theory (DFT) method at the B3LYP/6-311G(d,p) level, using the Gaussian 16 program suite. The effect of THF was modeled using IEFPCM.

2.2. Hole transport in amorphous organic solids

The transport of holes in amorphous organic solids is governed by the hopping mechanism. The hopping rate (ω_{ij}) depends on the transfer integral (v_{ij}) between the hopping sites i and j, the HOMO difference (ΔE_{ij}) between them, and the reorganization energy (λ_{ht}) associated with hole transport. To determine λ_{ht}, we employed the density functional theory (DFT) method at the B3LYP/6-311G(d,p) level. Subsequently, using the Amorphous Cell in Materials Studio 8.0, we constructed a cubic box with periodic boundaries comprising 360 organic semiconductor molecules. Molecular dynamics (MD) simulations were performed using the COMPASS II force field to obtain the microstructure of the amorphous box. Neighbor lists were generated from the box, each containing a pair of molecules that satisfied the selection rule of a nearest atom-to-atom distance ≤ 5 Å. We extracted the centroid distance (d) of each neighbor list. For the evaluation of ΔE_{ij}, we utilized the Thole model to account for electrostatic and polarization contributions. The partial charges of the molecules in their neutral and cationic states were obtained through DFT calculations at the CAM-B3LYP/6-311G(d,p) level. The energetic disorder was determined using the Gaussian disorder model by fitting the profile of ΔE_{ij}. To compute v_{ij}, an approximate method based on ZINDO was applied to each neighbor list, producing consistent results with those obtained at the B3LYP/6-31G(d,p) level.[4] Finally, the VOTCA toolkit was utilized for stochastic kinetic Monte Carlo (kMC) simulations to determine the hole mobility.

2.3. Glass transition, diffusivity, and permeability

We constructed a cubic box with periodic boundaries using the Amorphous Cell in Materials Studio 8.0, comprising 360 organic semiconductor molecules and additional molecules of TBPHTFSI in a weight ratio of 85:15. Molecular dynamics (MD) simulations were then performed using the COMPASS II force field. To investigate the glass transition temperature (T_g) and diffusivity (D), we conducted simulations using the FORCITE module in Materials Studio 8.0. Initially, an NVT simulation with a Nose thermostat at 700 K was carried out, followed by an NPT simulation at the same temperature using

both a Nose thermostat and a Berendsen barostat. Subsequently, the temperature was systematically decreased from 700 K to 200 K at intervals of 20 K, and NVT and NPT simulations were performed at each temperature. The equilibrated specific volume (SV) was recorded and subjected to linear fitting. The theoretical T_g, denoted as T_g^{SV}, was determined by identifying the intersection of the resulting lines in the low and high temperature regions. Furthermore, we introduced additional H_2O or HI molecules to a TBPHTFSI-containing composite and conducted NVT and NPT simulations. Mean square displacements of intrinsic and extrinsic species were extracted by recording their trajectories to obtain D. The Sorption module in Materials Studio 8.0 was employed to perform a grand canonical Monte Carlo simulation, obtaining the adsorption isotherm and solubility coefficient (S) of H_2O or HI in the amorphous box. Finally, the permeability of gas molecules (P) was determined using the formula $P = D \times S$.

3. References

1 H. Xiang, W. Fan, J. H. Li, T. Li, N. Robertson, X. Song, W. Wu, Z. Wang, W. Zhu and H. Tian, *ChemSusChem*, 2017, **10**, 938.

2 T.-Y. Li, C. Su, S. B. Akula, W.-G. Sun, H.-M. Chien and W.-R. Li, *Org. Lett.*, 2016, **18**, 3386.

3 Y. Ren, M. Ren, X. Xie, J. Wang, Y. Cai, Y. Yuan, J. Zhang and P. Wang, *Nano Energy*, 2021, **81**, 105655.

4 V. Rühle, A. Lukyanov, F. May, M. Schrader, T. Vehoff, J. Kirkpatrick, B. Baumeier and D. Andrienko, *J. Chem. Theory Comput.*, 2011, **7**, 3335.

4. Additional data
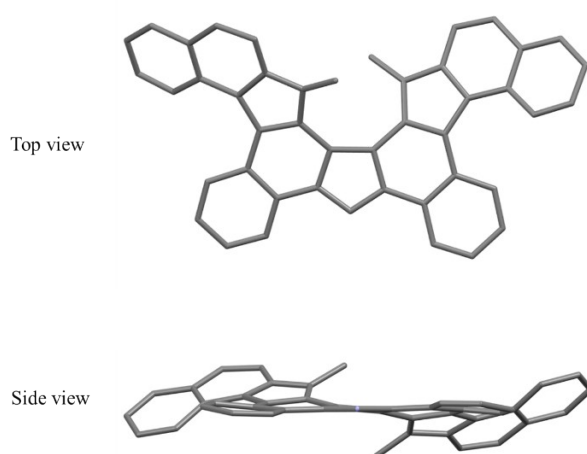
Fig. S1 Top-view and side-view of DMDAP from X-ray crystallographic analysis.

Table S1 Single crystal data of DMDAP

Compound	DMDAP
Empirical formula	$C_{42}H_{27}N_3$
Formula weight	717.87
Temperature	170 K
Wavelength [Å]	0.71073
Crystal system	Monoclinic
Space group	$P\,21/c$
a [Å]	10.8046 (4)
b [Å]	22.2850 (7)
c [Å]	15.2955 (4)
α [°]	90
β [°]	92.948 (1)
γ [°]	90
Volume [Å³]	3678.0 (2)
Z	4
ρ_{calc} [g cm⁻³]	1.296
μ [mm⁻¹]	0.079
F [000]	1520.0
Crystal size [mm³]	0.13×0.28×0.19
Radiation	MoKα ($\lambda = 0.71073$)
2Θ range for data collection [°]	2.43 to 27.04
CCDC deposition number	2195841
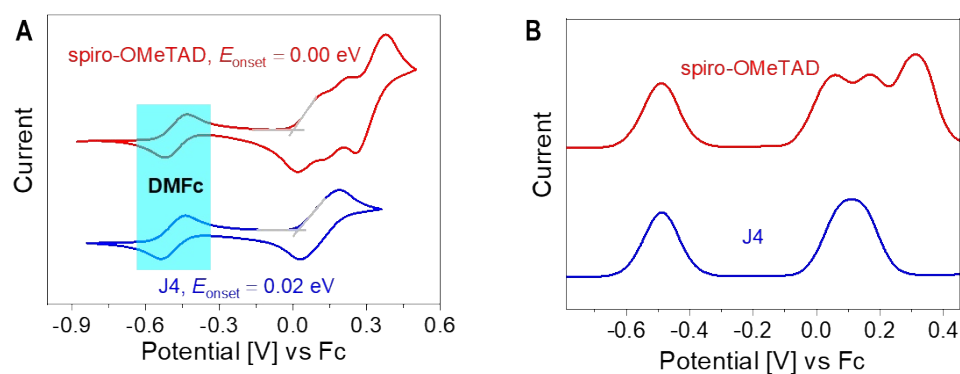
Fig. S2 (A) Cyclic voltammograms of spiro-OMeTAD and J4, using bis(pentamethylcyclopentadienyl)iron (DMFc) as the internal reference. The derived onset potential (E_{onset}) of the first oxidation wave is also presented. (B) Square wave voltammograms of spiro-OMeTAD and J4.
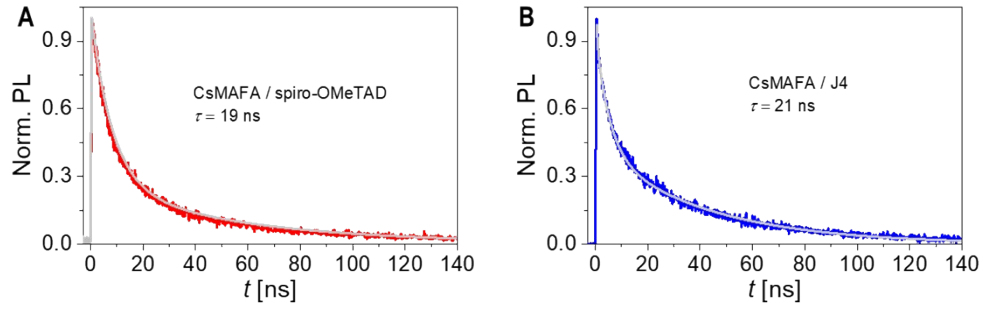
Fig. S3 Time-resolved photoluminescence (PL) traces of CsMAFA perovskite films with and without an organic semiconductor layer. The gray lines represent the biexponential fits of normalized PL as a function of time (t), yielding the amplitude-averaged lifetime (τ). The excitation wavelength is 670 nm.

Table S2 Fitting parameters, amplitude-averaged time constants, and hole extraction yields[a]

sample	τ_1 [ns]	A_1	τ_2 [ns]	A_2	τ [ns]	ϕ_{he} [%]
glass/CsMAFA	818	0.15	2702	0.85	2419	/
glass/CsMAFA/spiro-OMeTAD	8	0.44	34	0.56	19	99.2
glass/CsMAFA/J4	5	0.55	40	0.45	21	99.1
glass/CsMAFA/TMDAP-OMeDPA	8	0.73	51	0.27	20	99.2
glass/CsMAFA/TMDAP-EP-OMeDPA	8	0.48	36	0.52	21	99.1

[a] The time-resolved photoluminescence decays were analyzed using a biexponential decay function. The fast and slow decays were characterized by the time constants τ_1 and τ_2, respectively, while the relative amplitudes were denoted by A_1 and A_2. The amplitude-averaged time constant, denoted as τ, can be computed using the equation $\tau = A_1 \times \tau_1 + A_2 \times \tau_2$. Additionally, the yield of hole extraction (ϕ_{he}) was determined using the equation $\phi_{he} = 1 - \tau_w / \tau_{w/o}$, $\tau_{w/o}$ represents the amplitude-averaged time constant of CsMAFA without hole transport layer, and τ_w corresponds to the amplitude-averaged time constant of CsMAFA covered with hole transport layer.
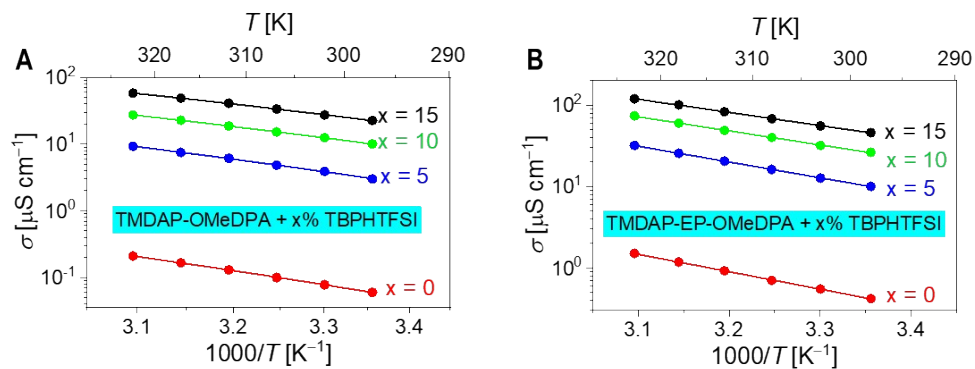
Fig. S4 (A,B) Arrhenius plots of electrical conductivity (σ) for thin films of molecular semiconductors with varying weight percentages of TBPHTFSI. T denotes the temperature in Kelvin.
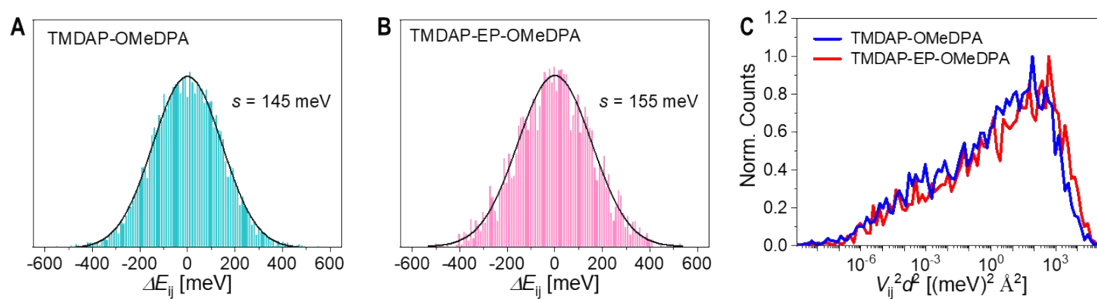
Fig. S5 (A,B) Statistical analysis of HOMO energy level difference (ΔE_{ij}). The energetic disorder (s) is also presented.

(C) Statistical analysis of the square of the product of transfer integral and centroid distance ($v_{ij}^2 d^2$).
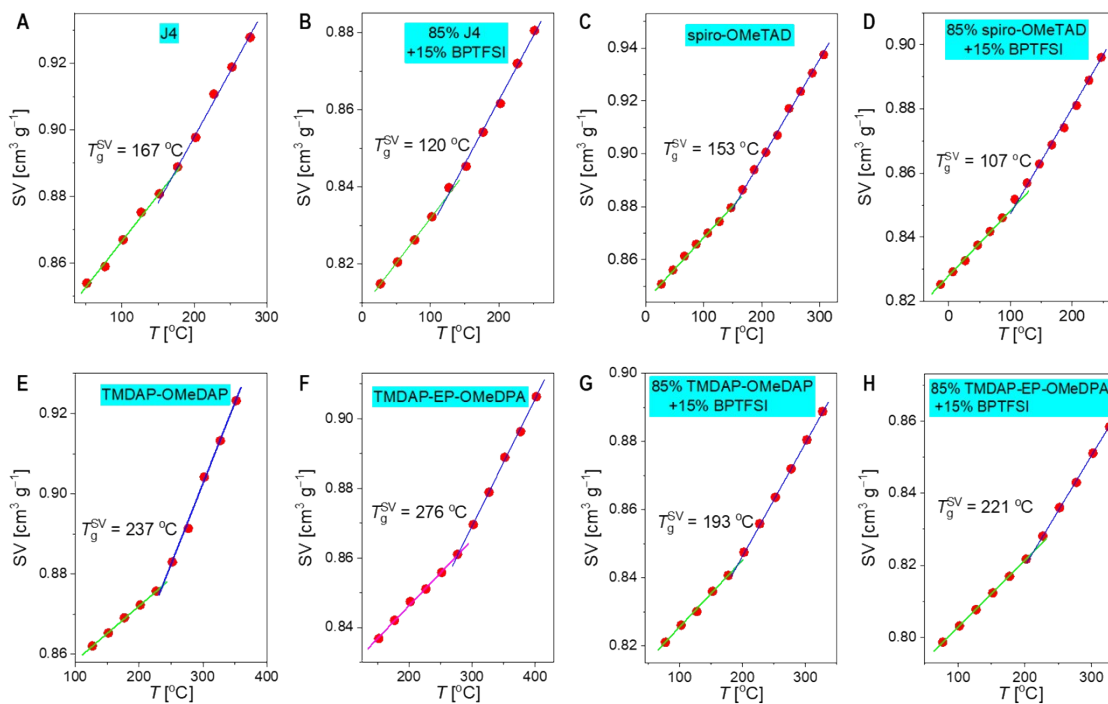
Fig. S6 Plots of specific volume (SV) as a function of temperature (T), obtained from molecular dynamics simulation. The green and blue lines depict the linear fits of the low-temperature and high-temperature regions, respectively. The theoretical glass transition temperature (T_g^{SV}) can be determined by the intersection of the linear fits.
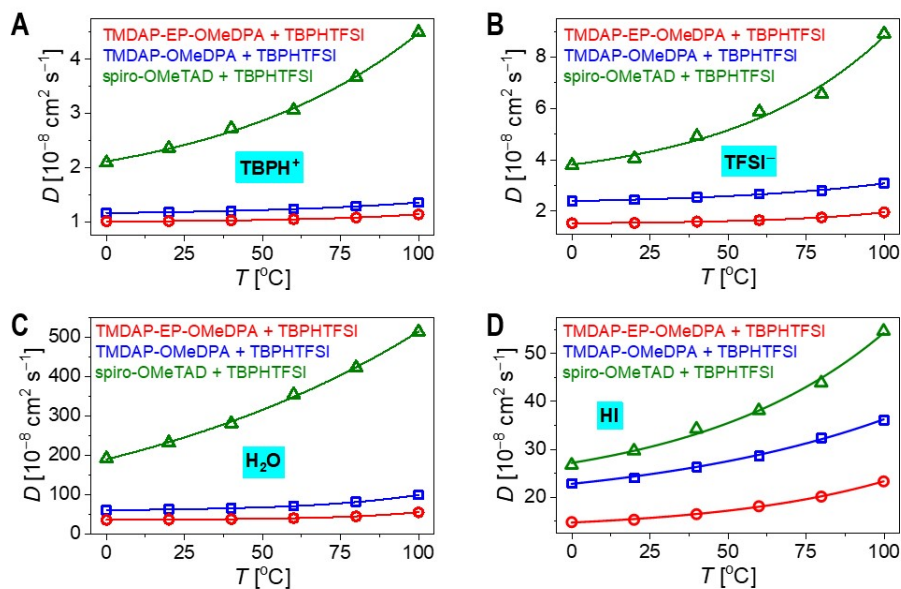
Fig. S7 (A–D) Temperature-dependent diffusivities (D) for internal and external species in organic semiconductor composites containing 15 wt% TBPHTFSI: (A) TBPH$^+$; (B) TFSI$^-$; (C) H_2O; (D) HI.
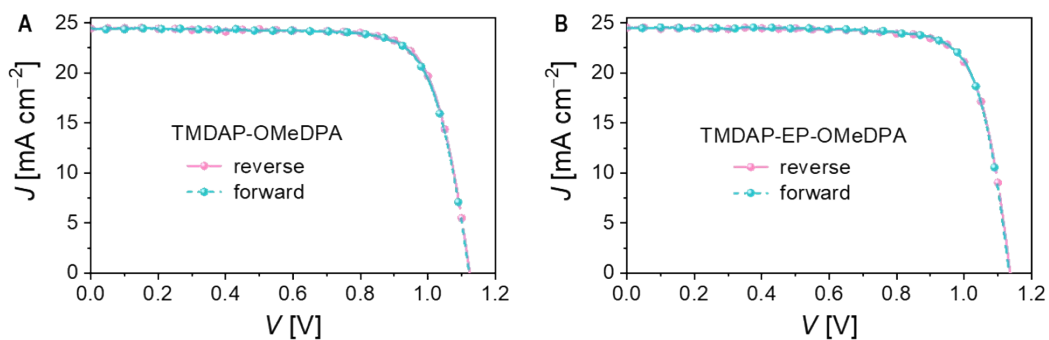
Fig. S8 *J–V* curves at the forward and reverse scans of representative PSCs with (A) TMDAP-OMeDPA and (B) TMDAP-EP-OMeDAP, under irradiation of AM1.5G simulated sunlight (100 mW cm^{-2}). Scan rate: 50 mV s^{-1}.

J_{SC}	V_{OC}	FF	PCE
[mA cm^{-2}]	[V]	[%]	[%]
24.50	1.120	71.3	19.6
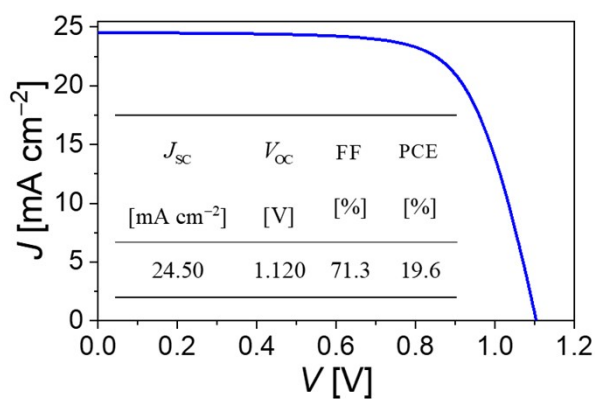
Fig. S9 Current density−voltage (*J*−*V*) characteristic of PSC with J4 measured under AM1.5G conditions. The performance parameters (short-circuit photocurrent density, J_{sc} ; open-circuit photovoltage, V_{oc} ; fill factor, FF ; power conversion efficiency, PCE) were also presented.
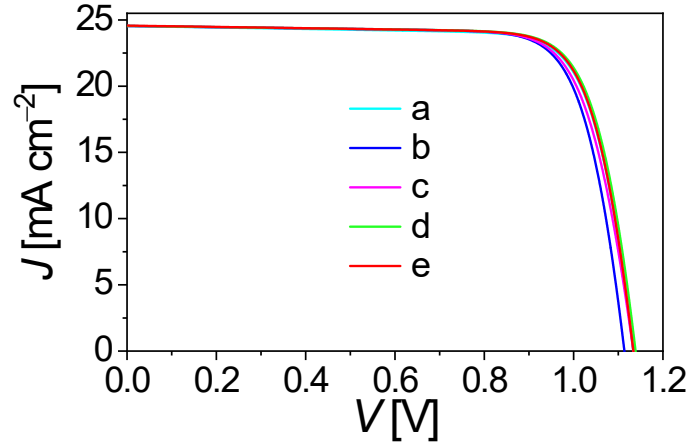
Fig. S10 Simulation of J–V curves based on the Shockley diode equation to quantify the impact of individual parameters (R_{sh}, I_s, R_s, or n) on both V_{OC} and FF. To achieve this, we generated a new J–V curve by incorporating one fitting parameter (a) R_{sh}, (b) I_s, (c) R_s, or (d) n from the J–V data of the TMDAP-OMeDPA cell, maintaining the other three fitting parameters of the J–V data of the TMDAP-EP-OMeDPA cell. Curve (e) corresponds to the J–V data of the TMDAP-EP-OMeDPA cell and is presented for comparation.

Table S3 Parameters employed in J–V simulation and performance parameters inferred from simulated J–V characteristics[a]

Simulation parameters					Performance parameters			
R_{sh} [kΩ]	I_s [A]	R_s [Ω]	n	I_{ph} [10^{-3} A]	J_{SC} [mA cm^{-2}]	V_{OC} [V]	FF [%]	PCE [%]
11.0	4.2×10^{-13}	13.0	1.90	3.93	24.5	1.120	77.0	21.13
14.1	2.5×10^{-13}	9.5	1.87	3.93	24.5	1.135	78.2	21.75
11.0	2.5×10^{-13}	9.5	1.87	3.93	24.5	1.133	78.0	21.65
14.1	4.2×10^{-13}	9.5	1.87	3.93	24.5	1.113	77.9	21.24
14.1	2.5×10^{-13}	13.0	1.87	3.93	24.5	1.135	77.3	21.50
14.1	2.5×10^{-13}	9.5	1.90	3.93	24.5	1.139	78.2	21.82

[a]The simulation parameters and performance parameters derived from the simulated J–V characteristics of the TMDAP-OMeDPA cell are marked in blue, whereas the simulation parameters and performance parameters derived from the simulated J–V characteristics of the TMDAP-EP-OMeDPA cell are marked in red.
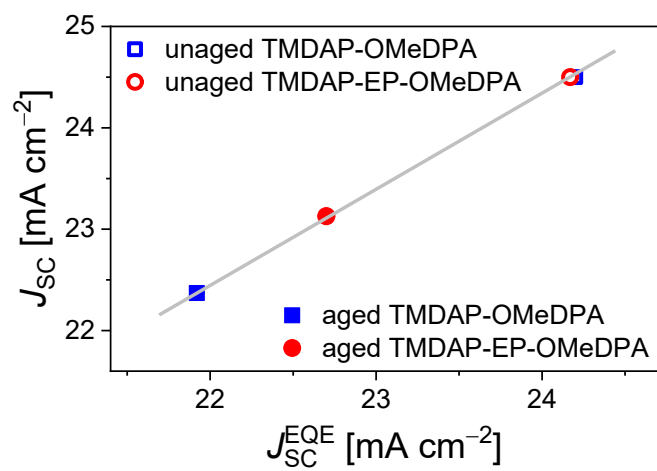
Fig. S11 Relation between photocurrent densities derived from photocurrent density–voltage curves (J_{SC}) and external quantum efficiency curves (J_{SC}^{EQE}).

5. APPENDIX: ¹H NMR, ¹³C NMR, MASS SPECTRA, AND IR SPECTRA
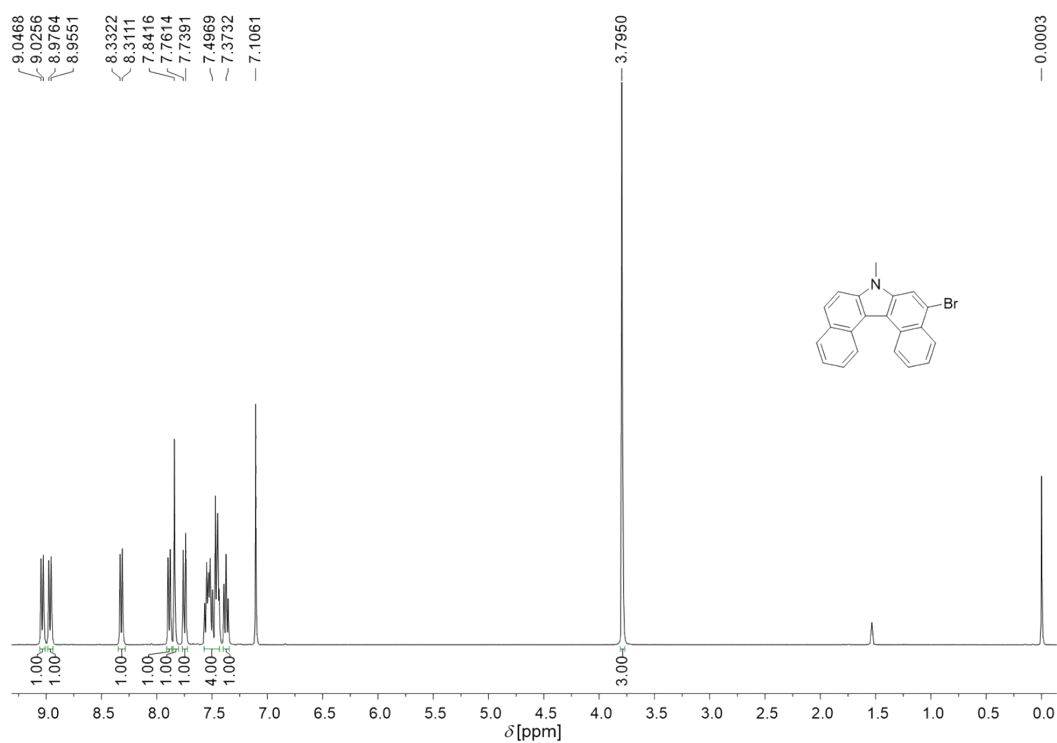
Fig. S12 ¹H NMR (400 MHz) spectrum of compound **2** in CDCl₃.
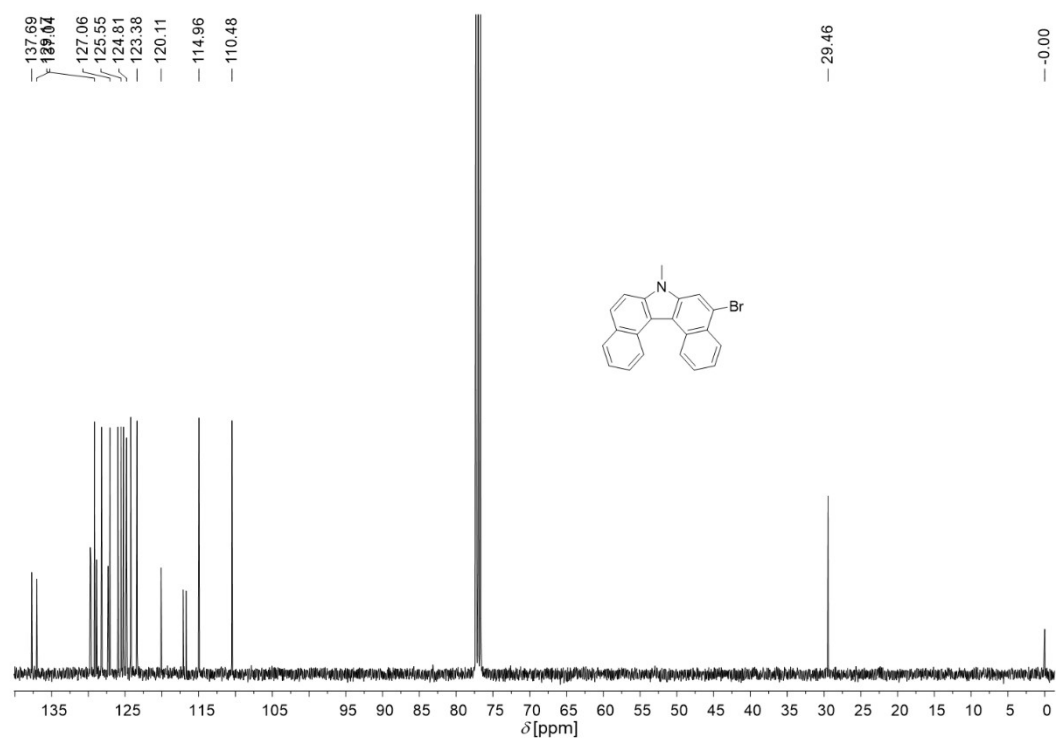
Fig. S13 ¹³C NMR (150 MHz) spectrum of compound **2** in CDCl₃.
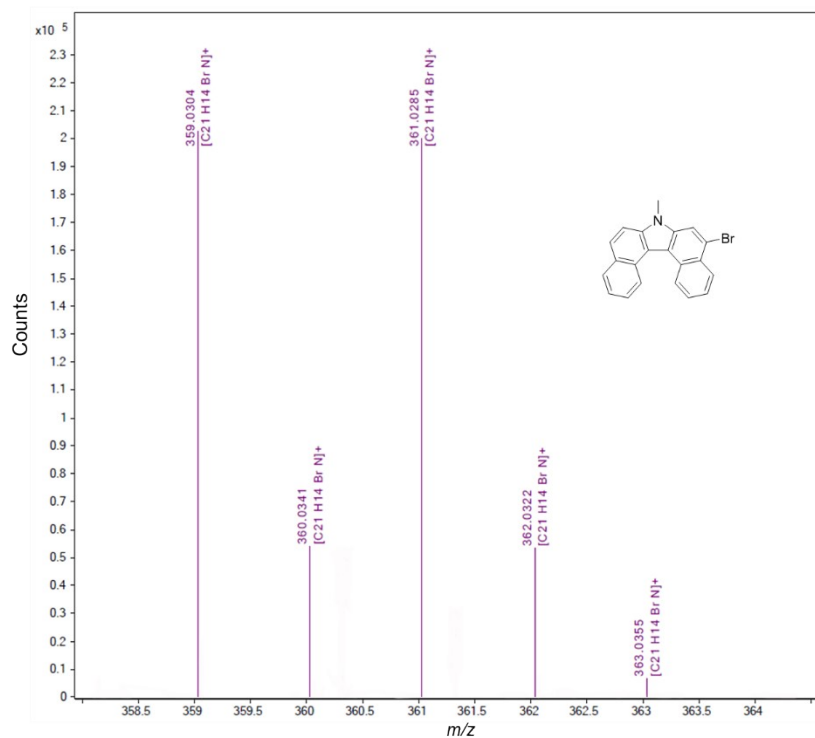
Fig. S14 High-resolution mass spectrum (ESI) of compound **2**.
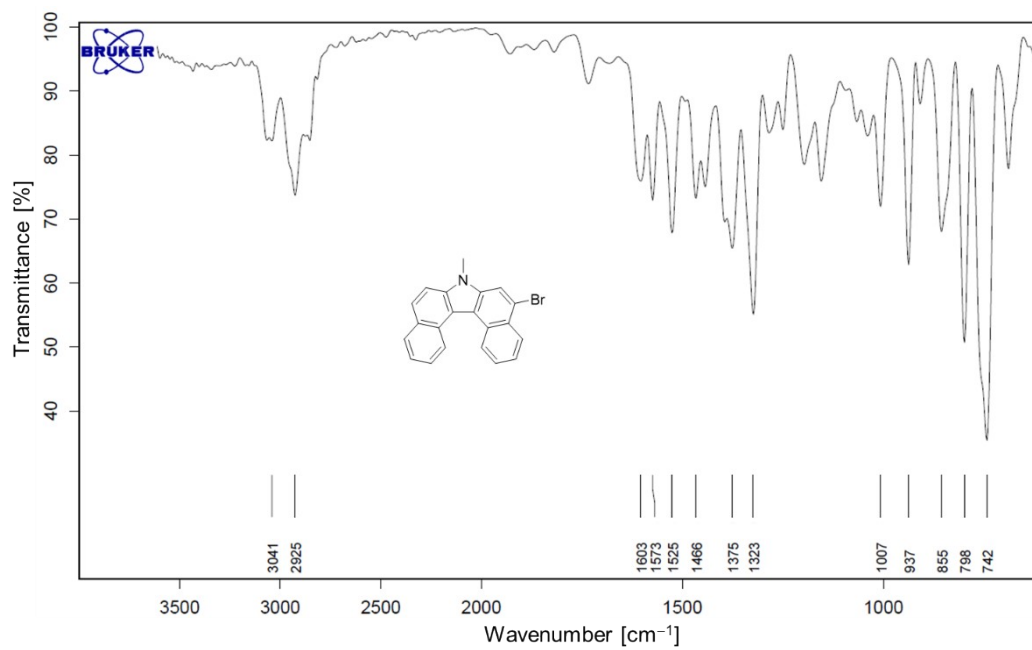
Fig. S15 ATR-FTIR spectrum of compound **2**.
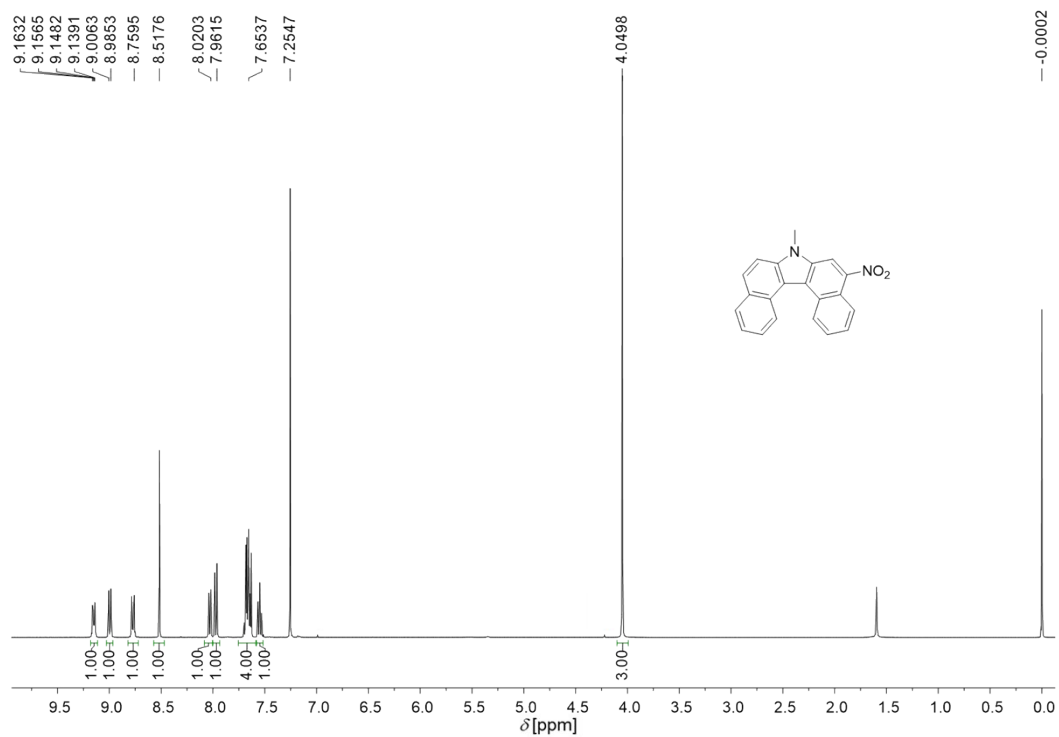
Fig. S16 ^{1}H NMR (400 MHz) spectrum of compound **3** in CDCl$_3$.
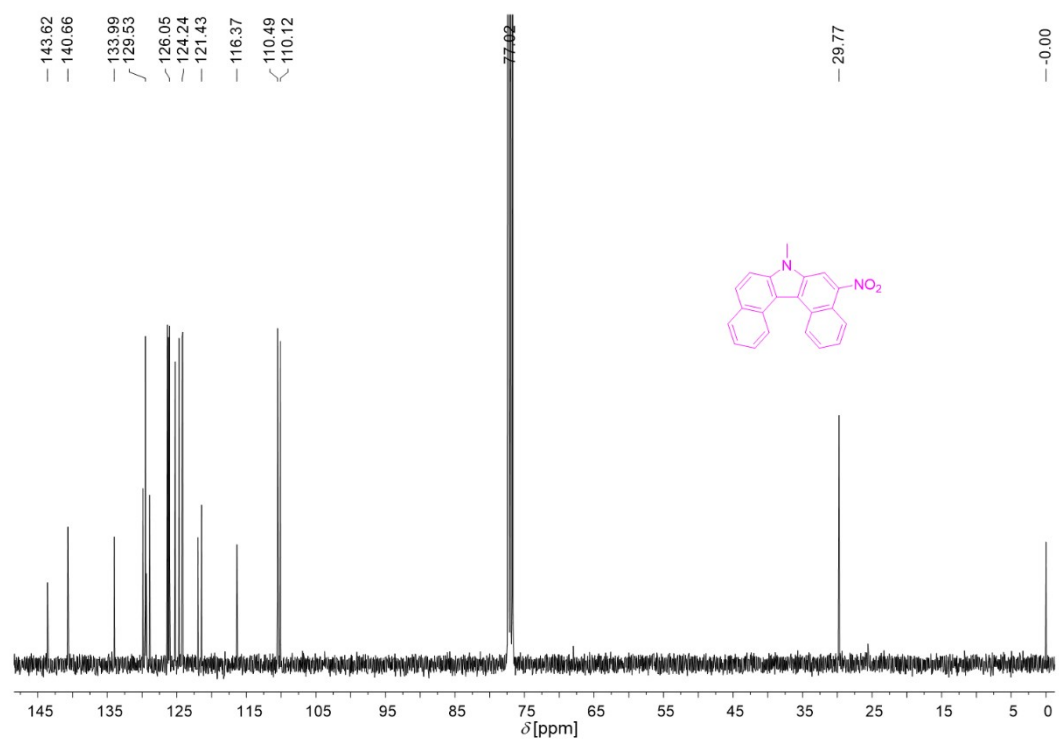
Fig. S17 ^{13}C NMR (100 MHz) spectrum of compound **3** in CDCl$_3$.
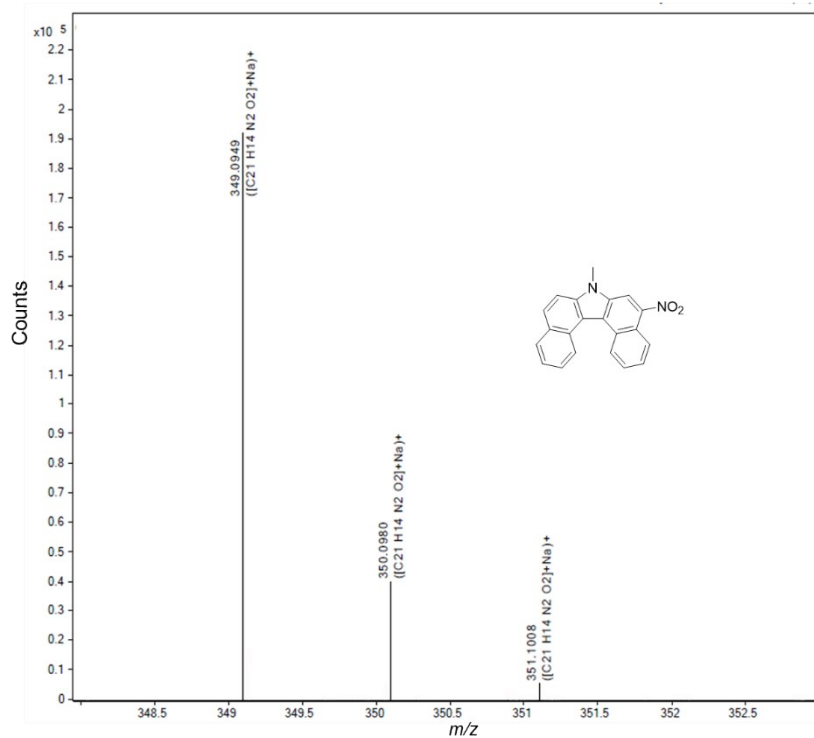
Fig. S18 High-resolution mass spectrum (ESI) of compound **3**.
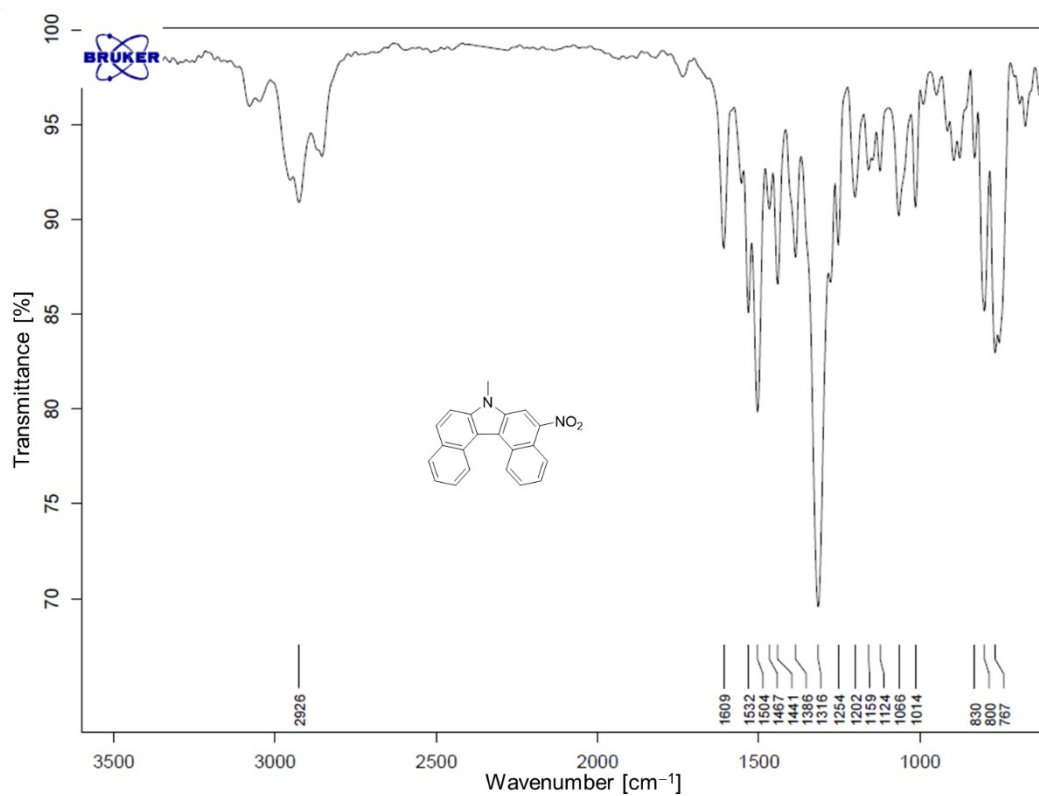
Fig. S19 ATR-FTIR spectrum of compound **3**.
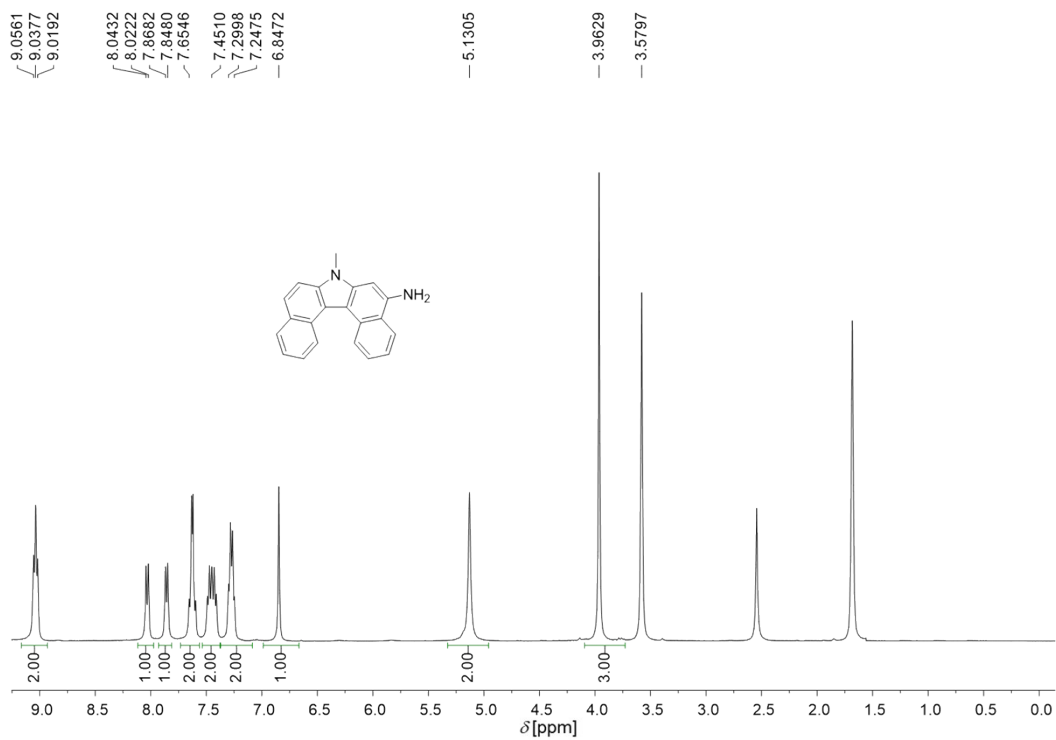
Fig. S20 ^{1}H NMR (400 MHz) spectrum of compound **4** in THF-d_8.
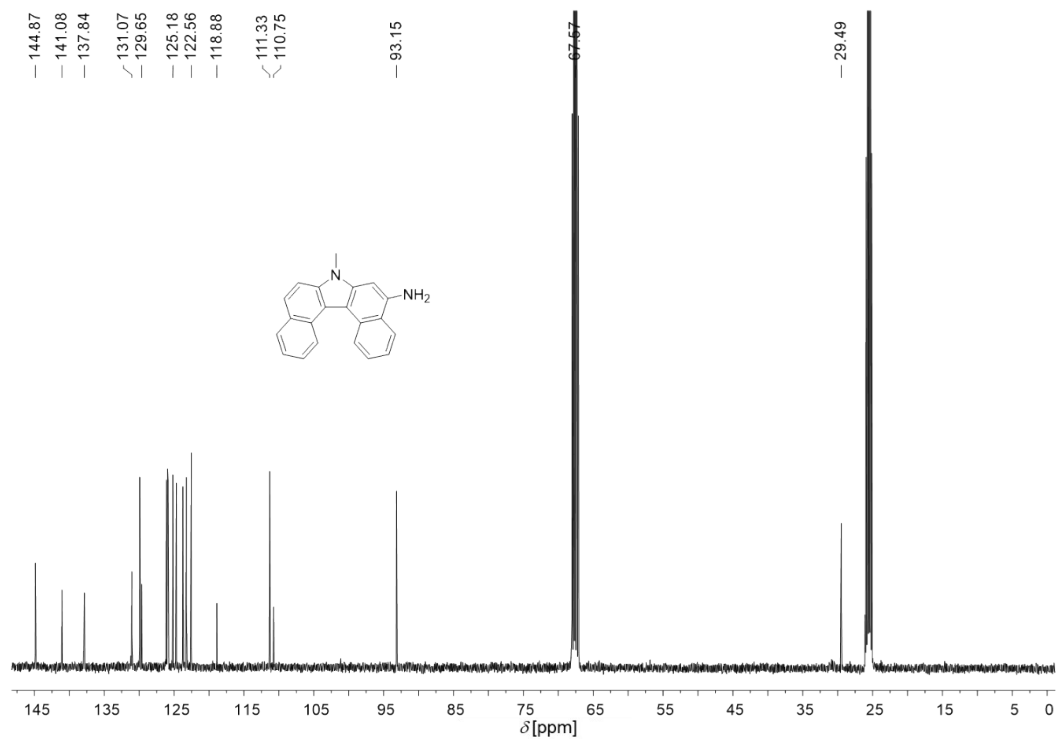
Fig. S21 ^{13}C NMR (100 MHz) spectrum of compound **4** in THF-d_8.
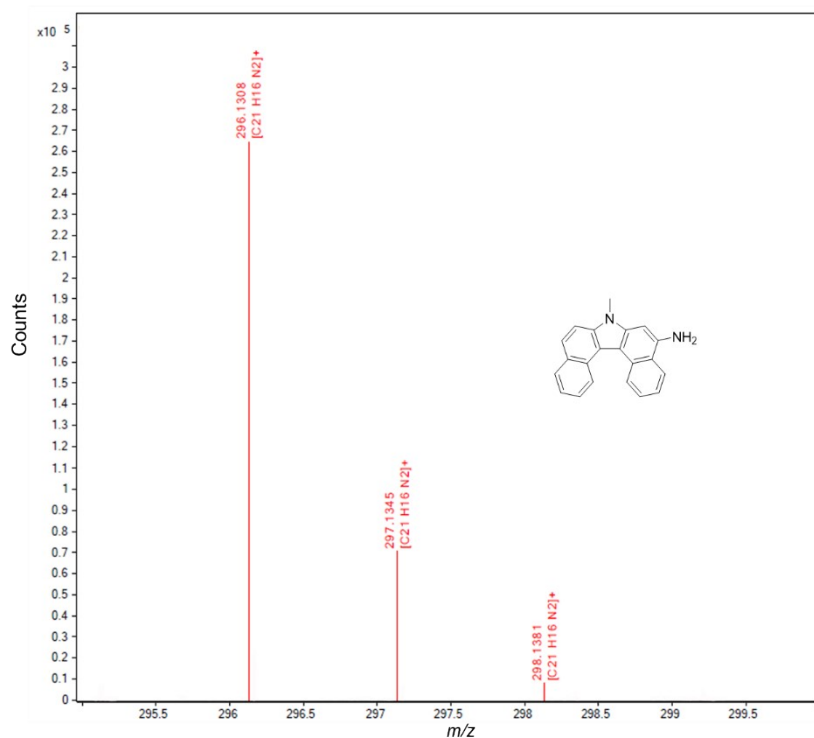
Fig. S22 High-resolution mass spectrum (ESI) of compound **4**.
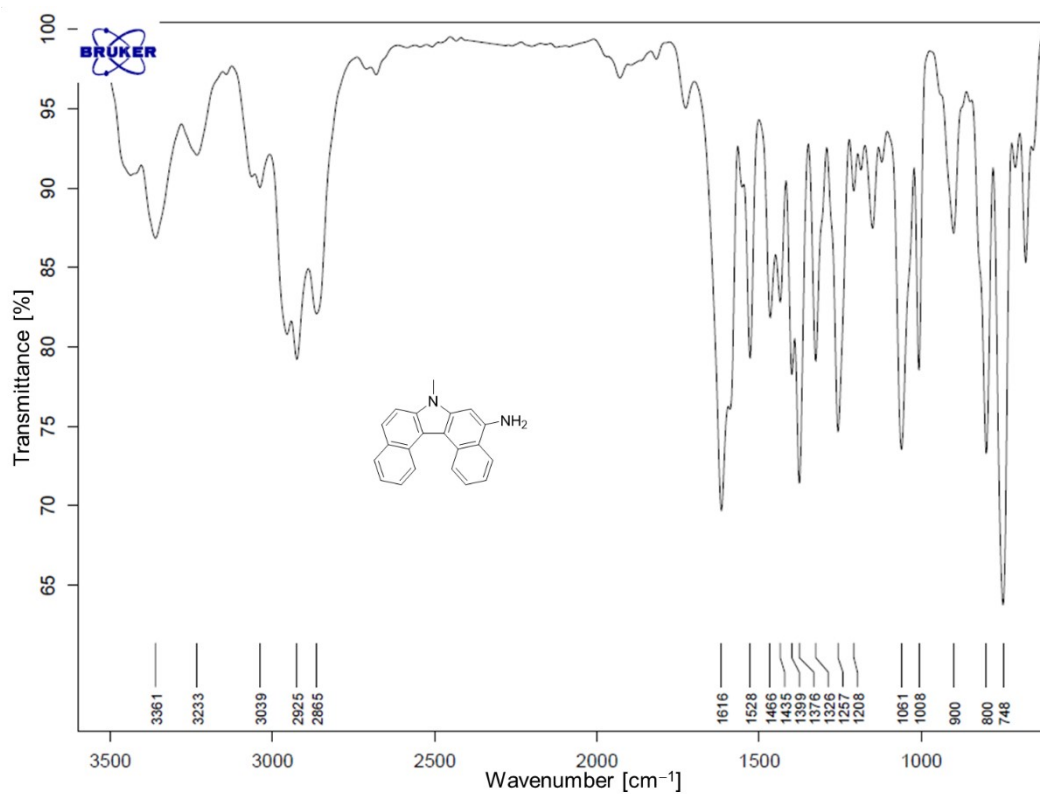
Fig. S23 ATR-FTIR spectrum of compound **4**.
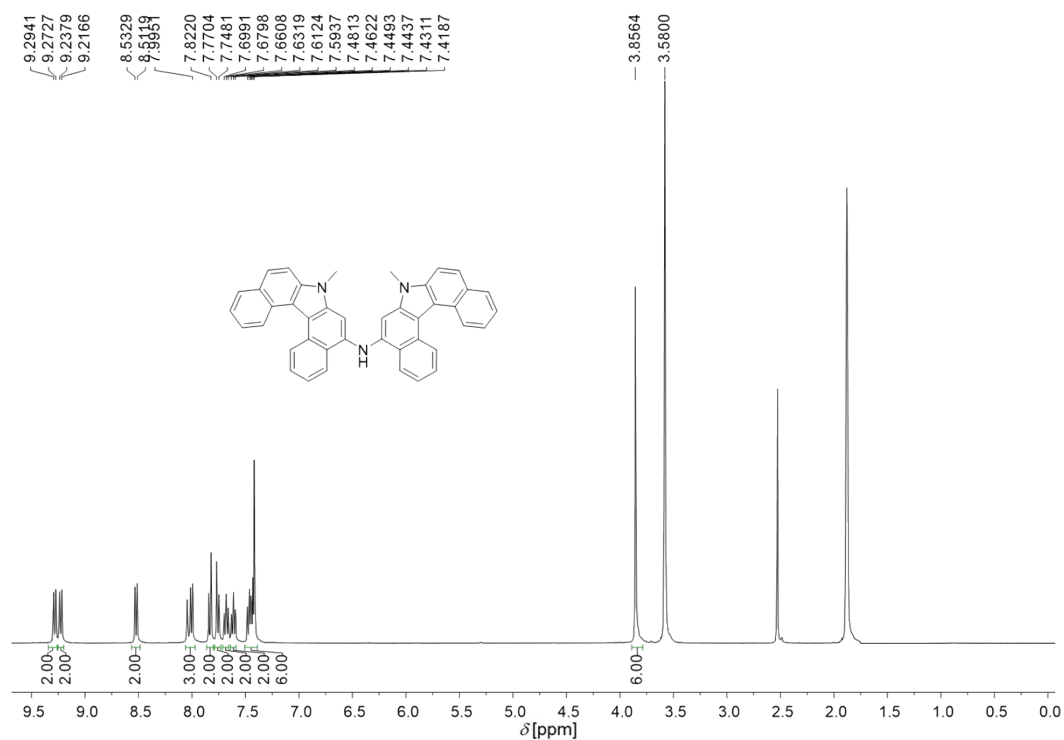
Fig. S24 ^{1}H NMR (400 MHz) spectrum of compound **5** in THF-d_8.
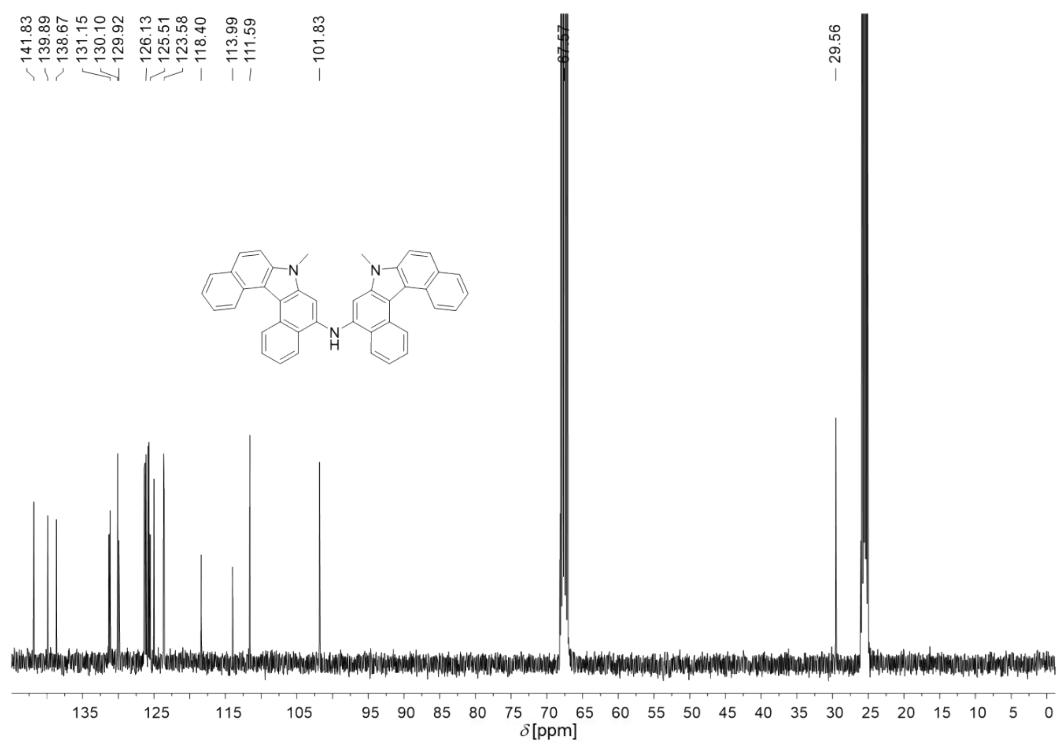
Fig. S25 ^{13}C NMR (100 MHz) spectrum of compound **5** in THF-d_8.
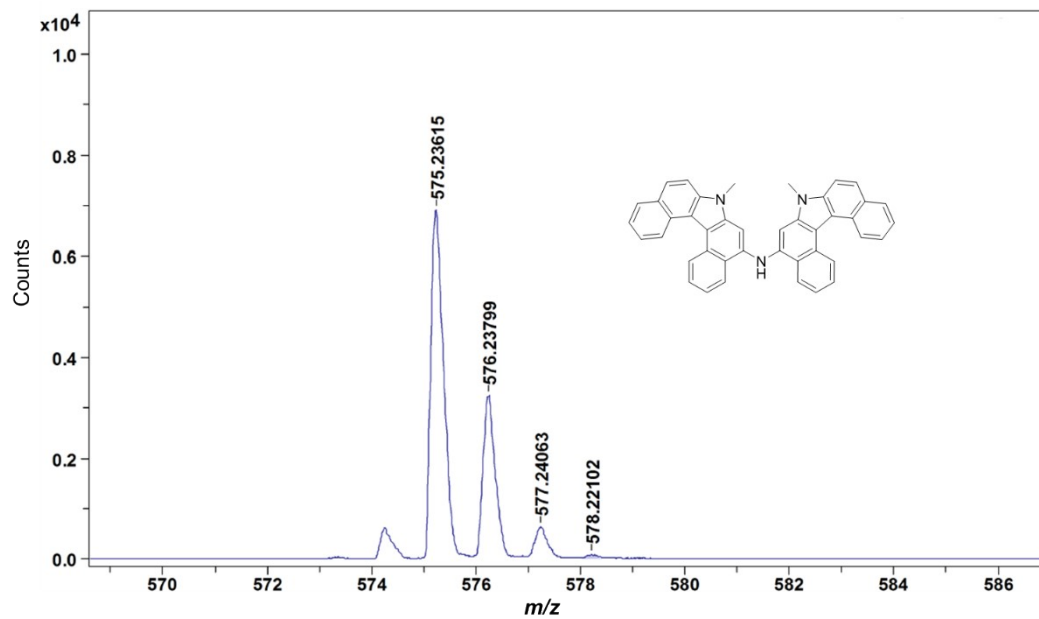
Fig. S26 MALDI-TOF mass spectrum of compound **5**.
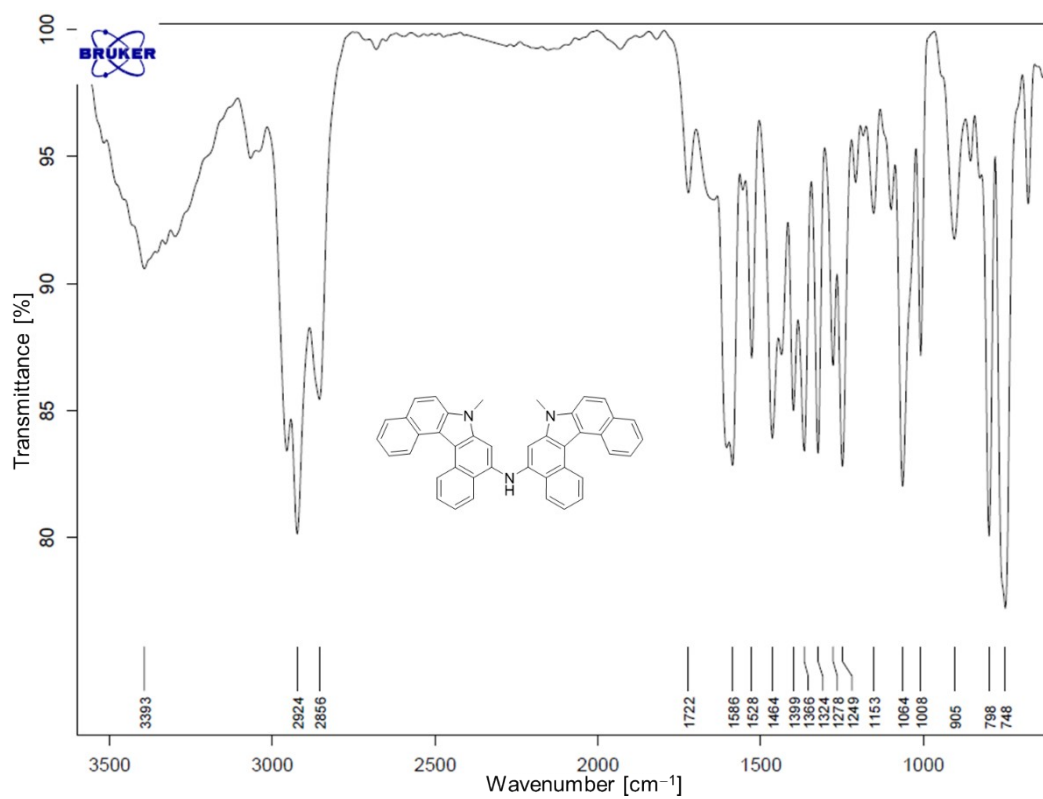
Fig. S27 ATR-FTIR spectrum of compound **5**.
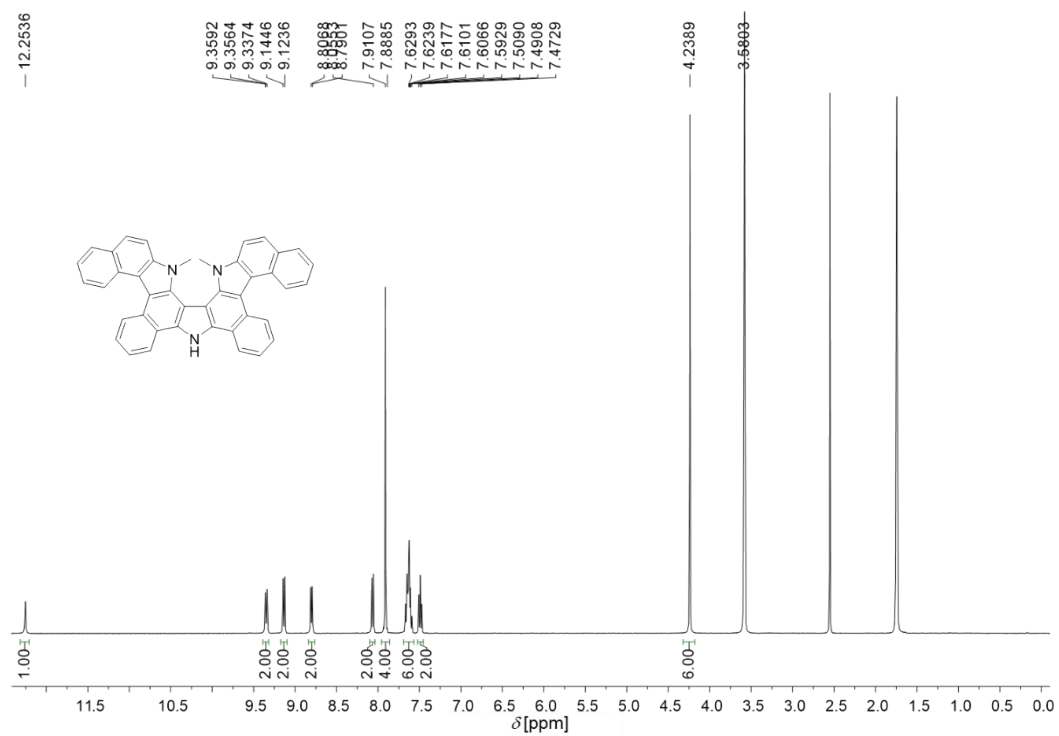
Fig. S28 ¹H NMR (400 MHz) spectrum of DMDAP in THF-d_8.
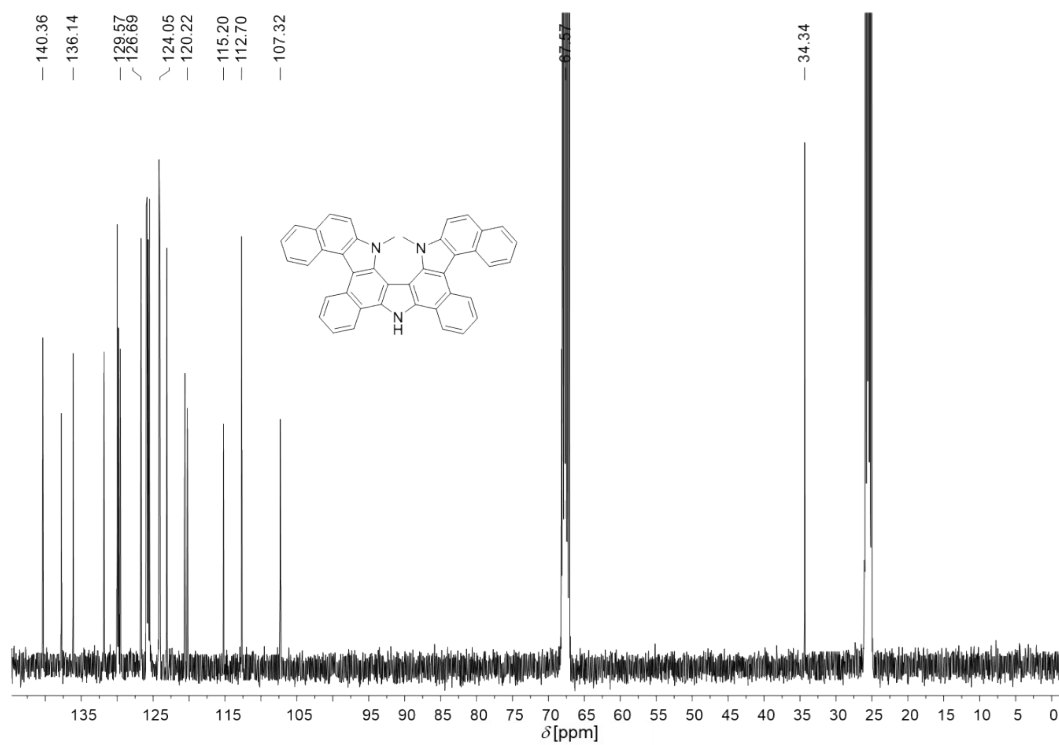
Fig. S29 ¹³C NMR (100 MHz) spectrum of DMDAP in THF-d_8.
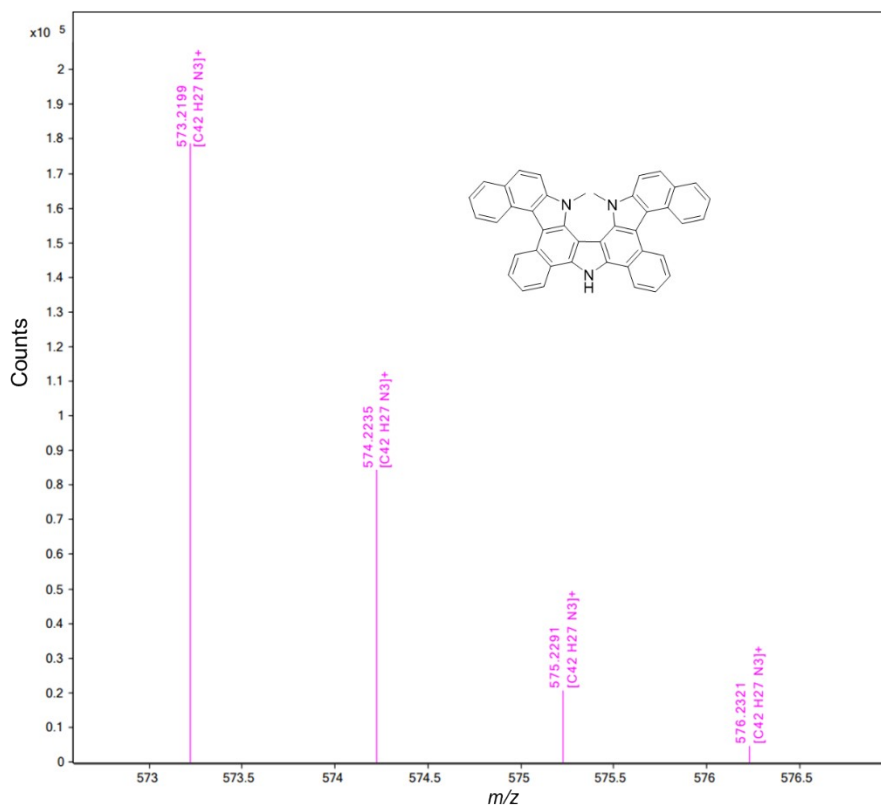
Fig. S30 High-resolution mass spectrum (ESI) of DMDAP.
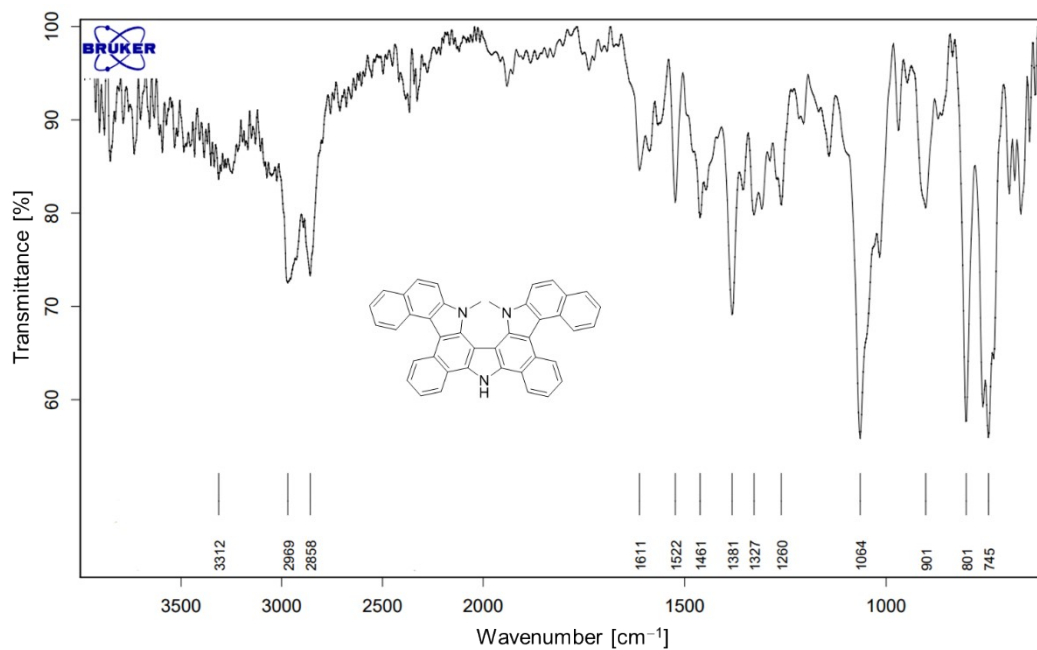
Fig. S31 ATR-FTIR spectrum of **DMDAP**.

Fig. S32 ^{1}H NMR (400 MHz) spectrum of TMDAP in THF-d_8.

Fig. S33 ^{13}C NMR (100 MHz) spectrum of TMDAP in THF-d_8.
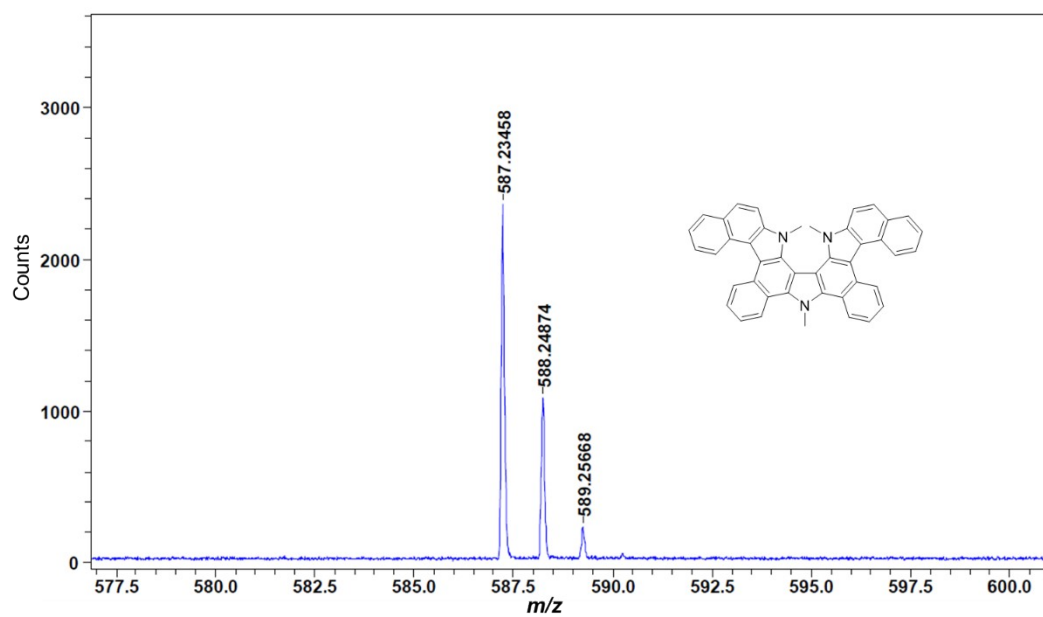
Fig. S34 MALDI-TOF mass spectrum of TMDAP.
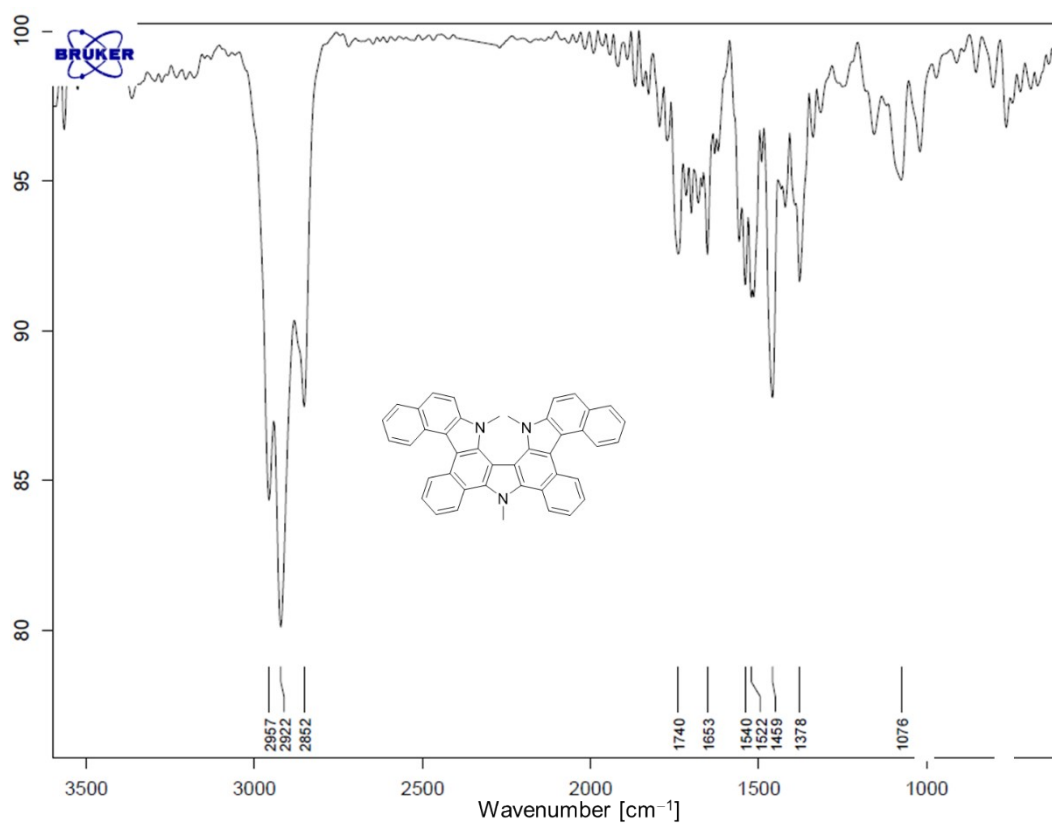
Fig. S35 ATR-FTIR spectrum of TMDAP.
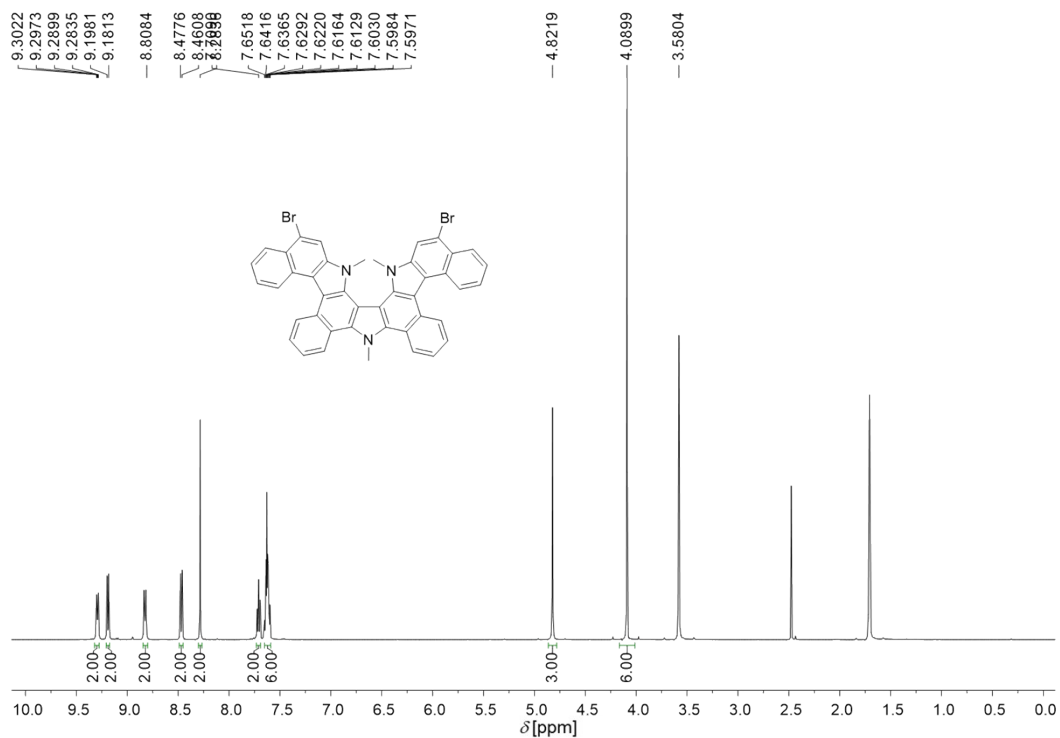
Fig. S36 ^{1}H NMR (400 MHz) spectrum of TMDAPBr$_2$ in THF-d_8.
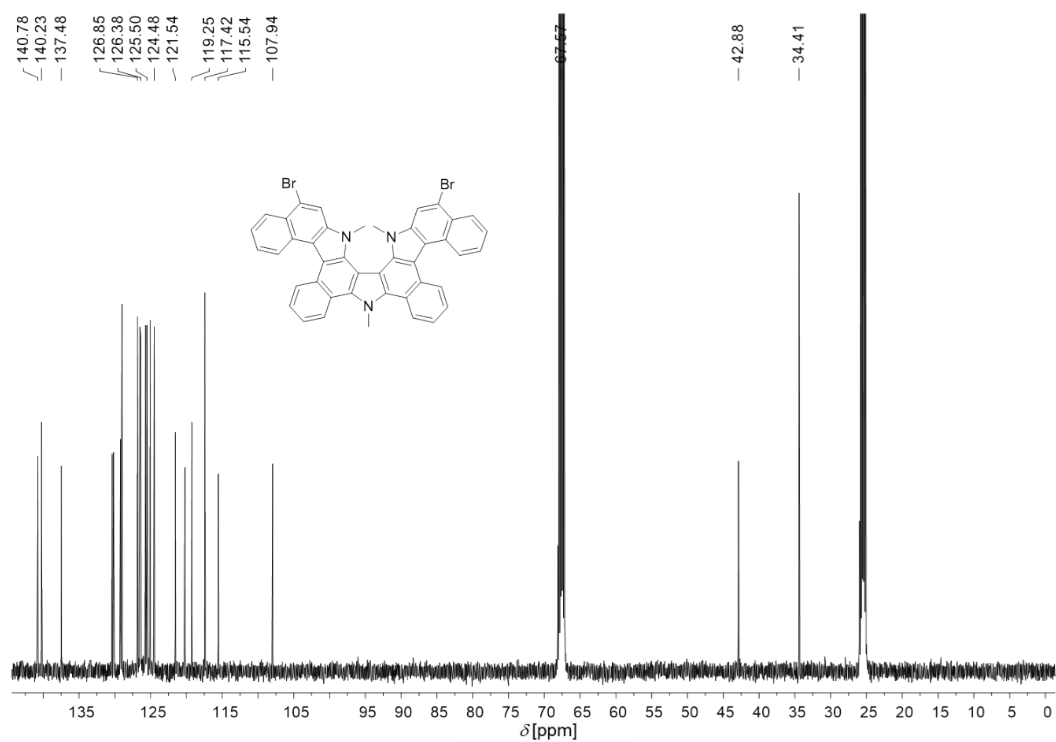
Fig. S37 ^{13}C NMR (100 MHz) spectrum of TMDAPBr$_2$ in THF-d_8.
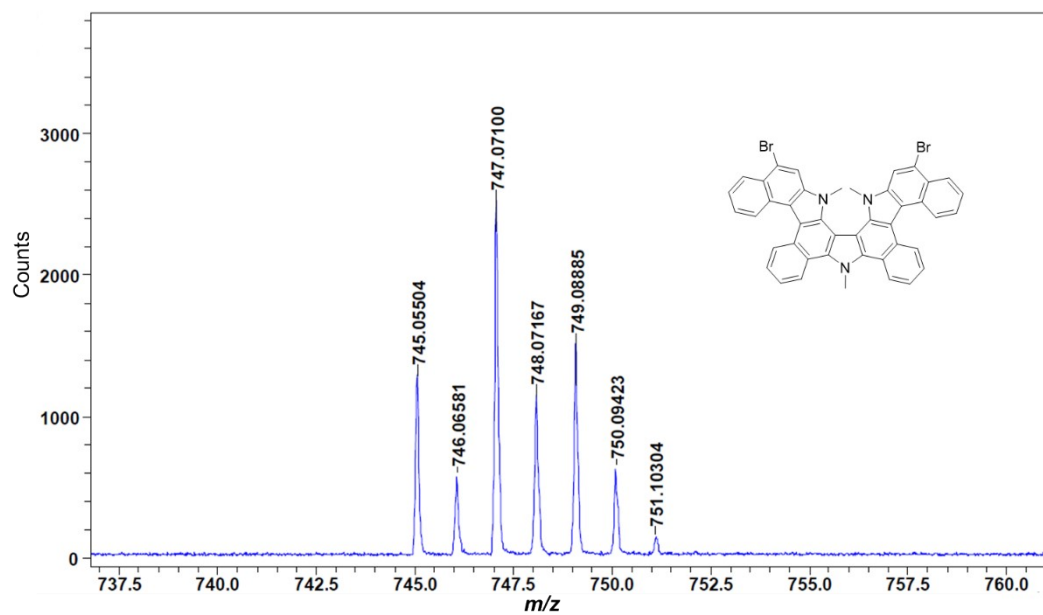
Fig. S38 MALDI-TOF mass spectrum of TMDAPBr$_2$.
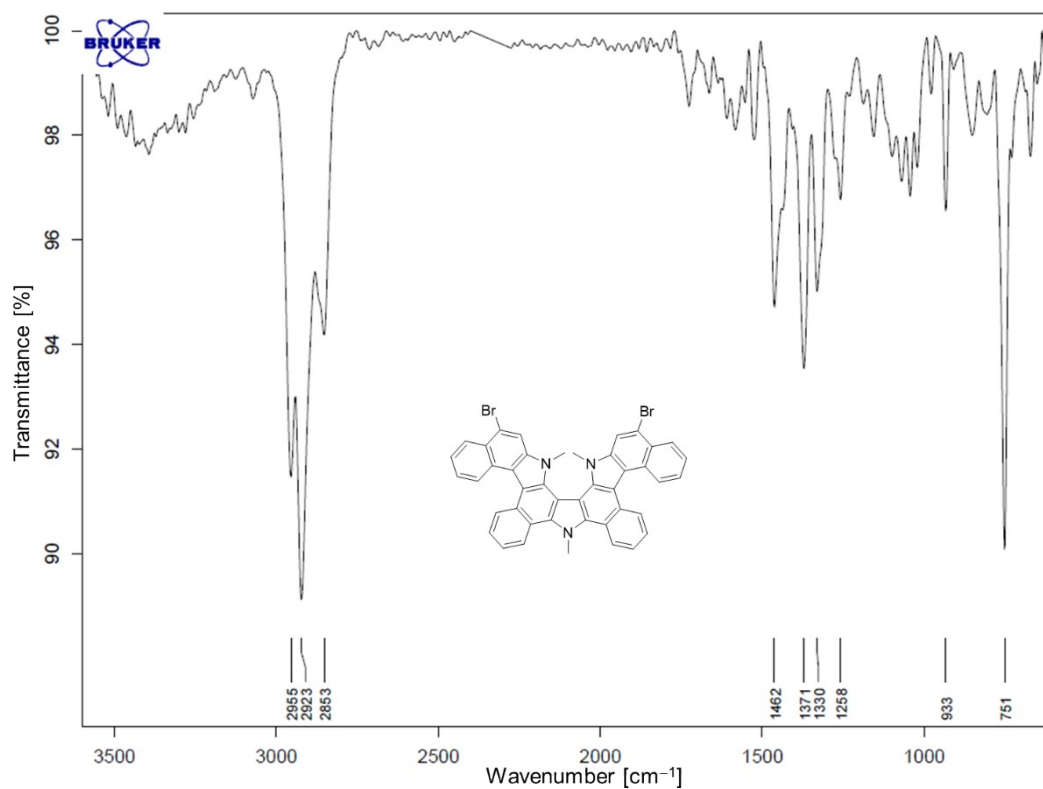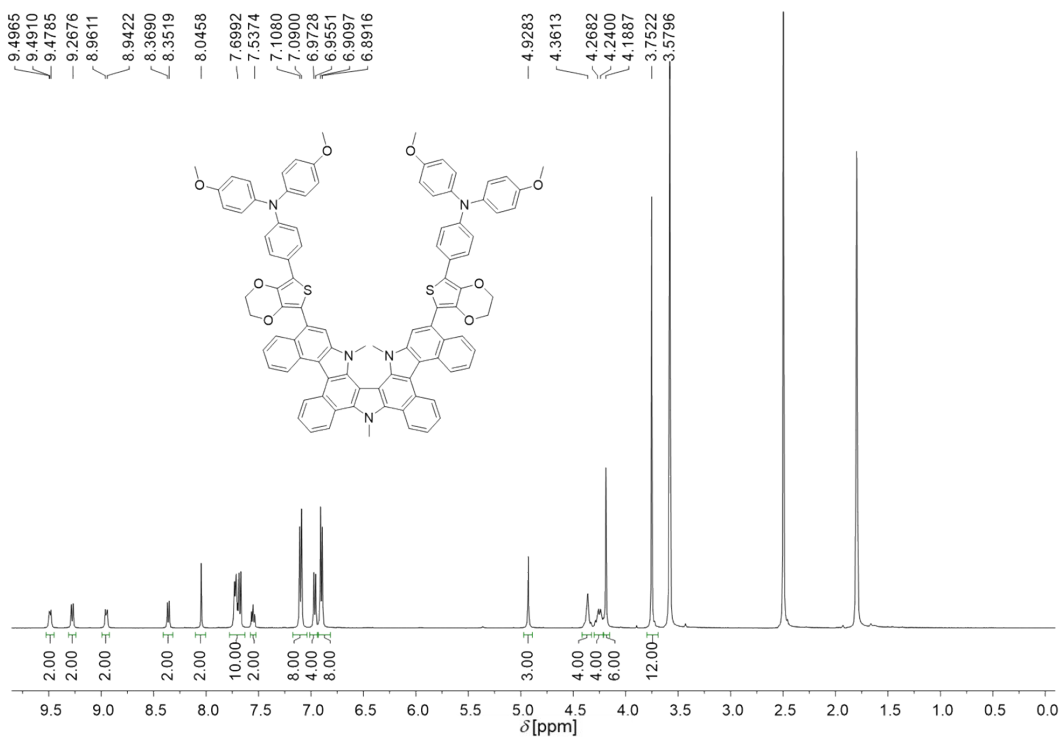

Fig. S39 ATR-FTIR spectrum of TMDAPBr$_2$.
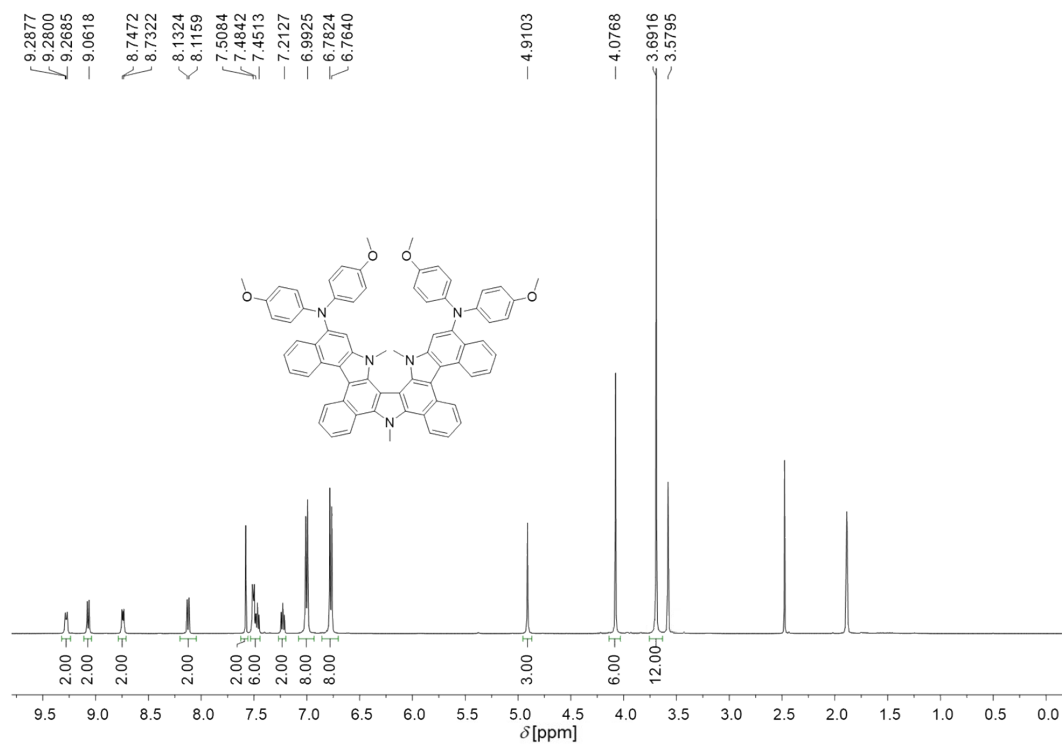
Fig. S40 ^{1}H NMR (400 MHz) spectrum of TMDAP-OMeDPA in THF-d_8.
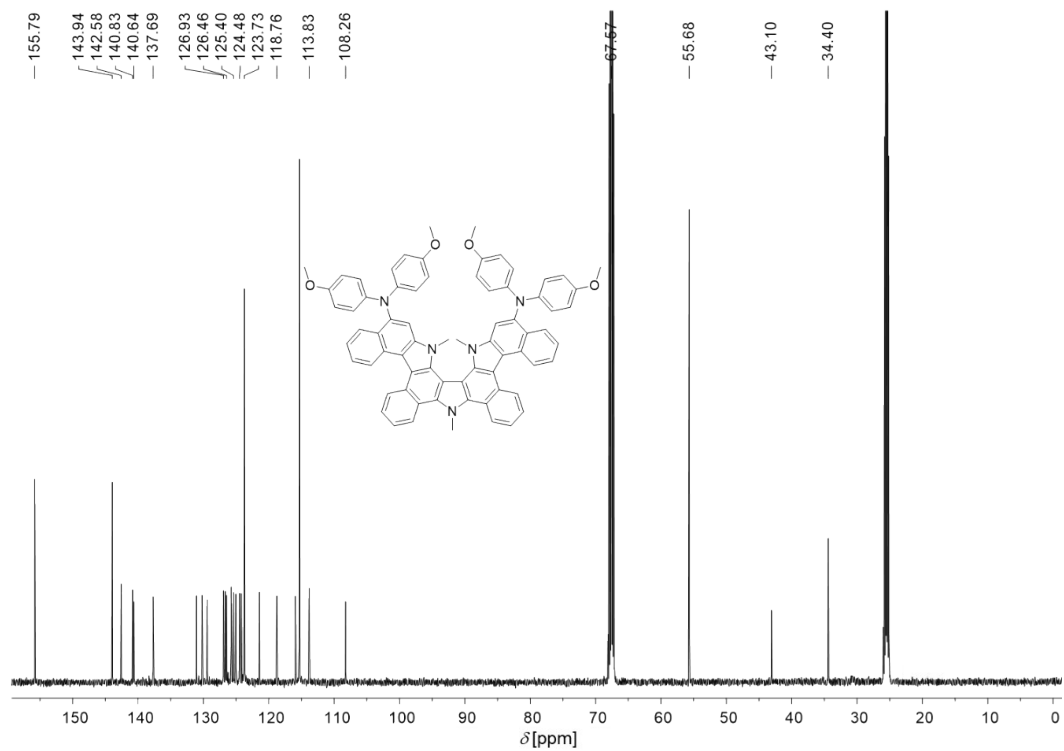
Fig. S41 ^{13}C NMR (100 MHz) spectrum of TMDAP-OMeDPA in THF-d_8.
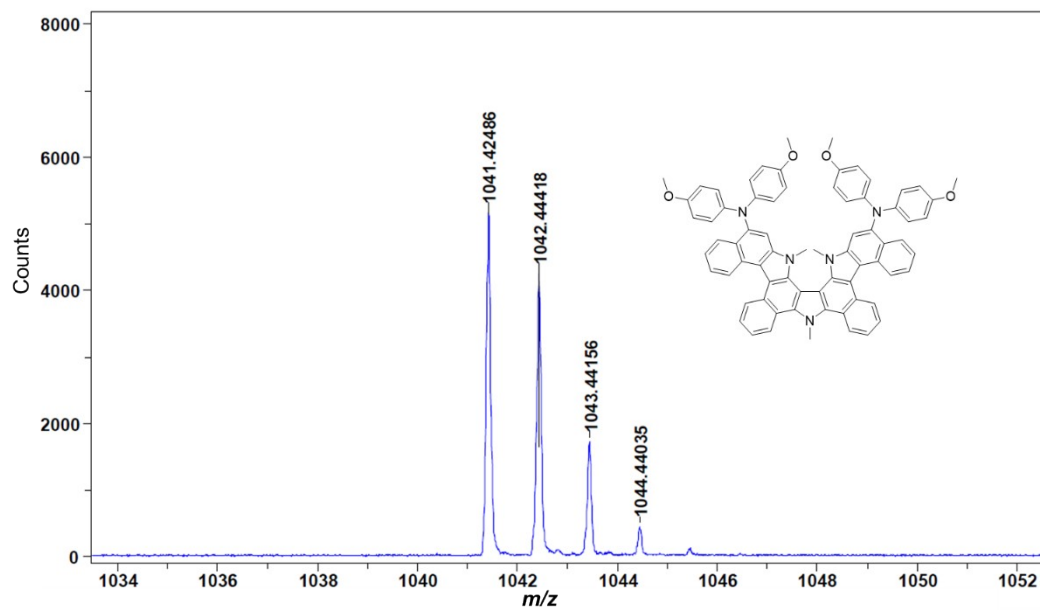
Fig. S42 MALDI-TOF mass spectrum of TMDAP-OMeDPA.
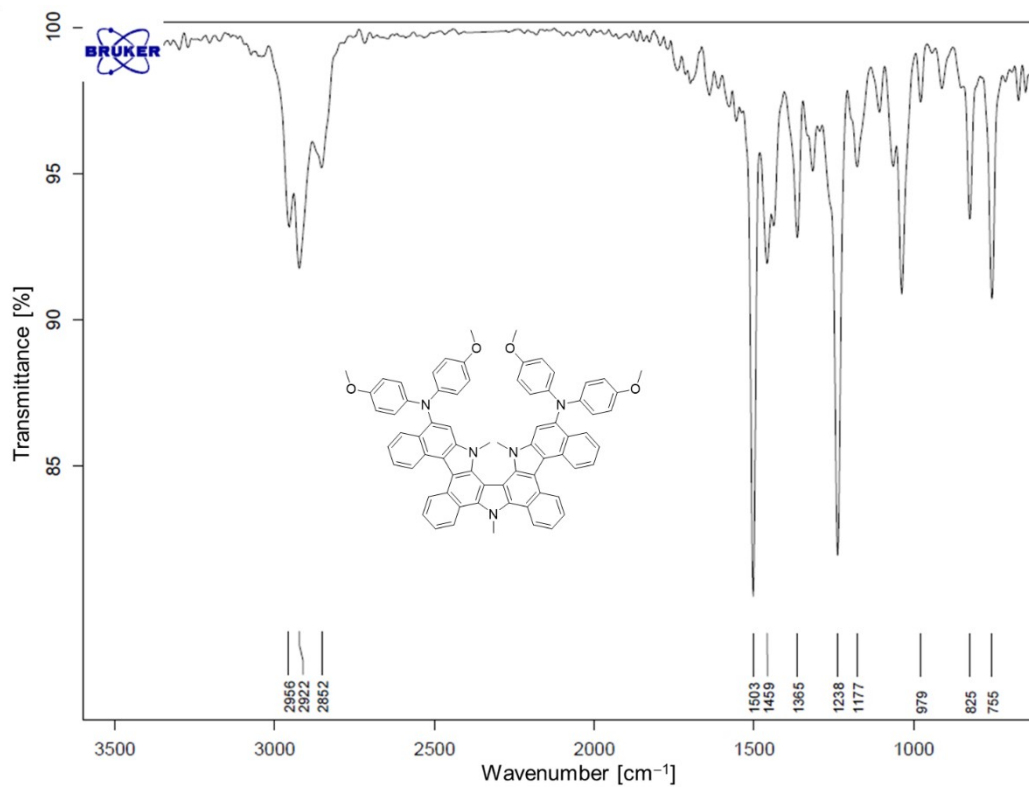
Fig. S43 ATR-FTIR spectrum of TMDAP-OMeDPA.

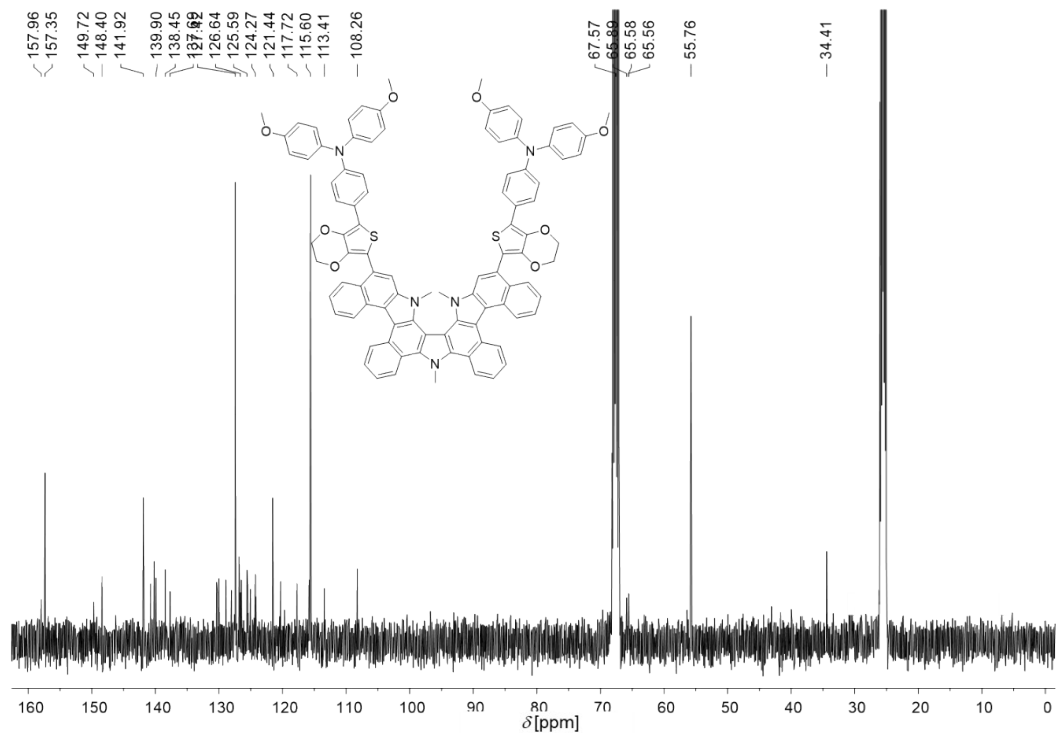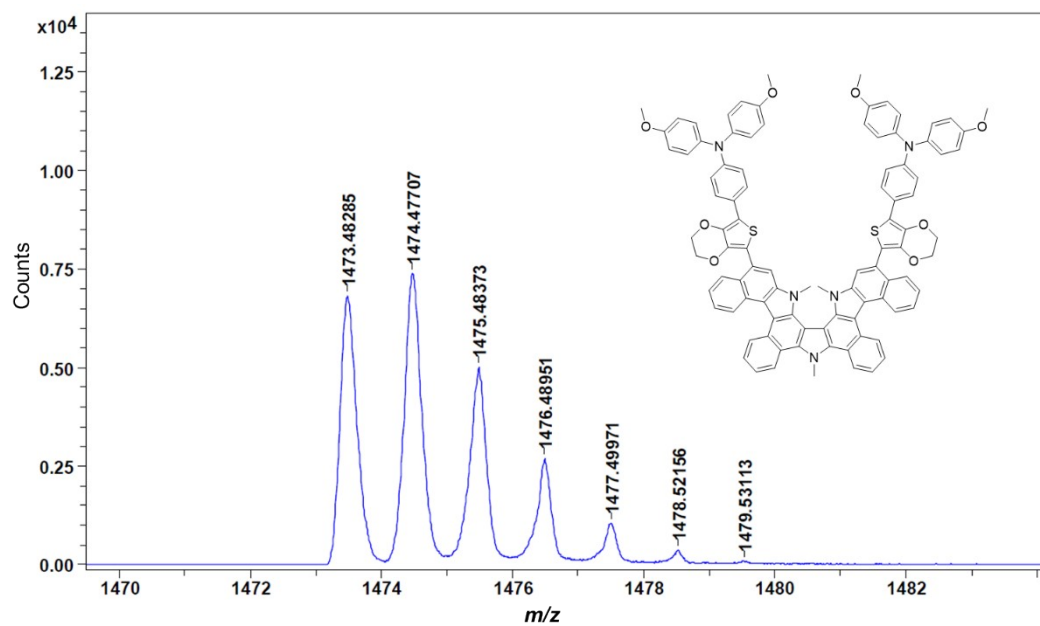**Fig. S44** ^{1}H NMR (400 MHz) spectrum of TMDAP-EP-OMeDPA in THF-d_8.

Fig. S45 ^{13}C NMR (100 MHz) spectrum of TMDAP-EP-OMeDPA in THF-d_8.
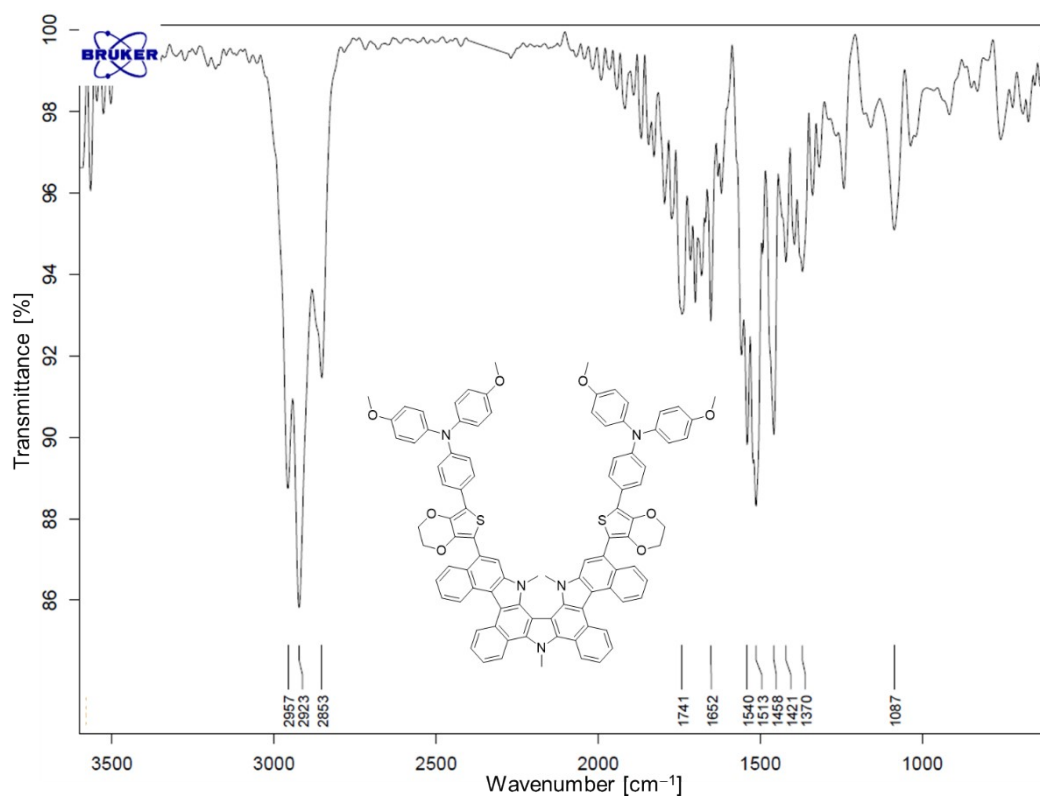
Fig. S46 MALDI-TOF mass spectrum of TMDAP-EP-OMeDPA.

Fig. S47 ATR-FTIR spectrum of TMDAP-EP-OMeDPA.